



Inhibition of CO₂ corrosion of mild steel – Study of mechanical effects of highly turbulent disturbed flow



Wei Li^{1,*}, B.F.M. Pots, Xiankang Zhong², Srdjan Nesic

Institute for Corrosion and Multiphase Technology, Department of Chemical and Biomolecular Engineering, Ohio University, Athens, OH 45701, United States

ARTICLE INFO

Keywords:

Acid inhibition
Mild steel
Wall shear stress
Cavitation
Polarization
Weight loss
SEM
CFD

ABSTRACT

The failure mechanisms of corrosion inhibitors in highly turbulent flow remain a disputed topic. In the present study, corrosion experiments of X65 pipeline steel were performed with an imidazoline-based corrosion inhibitor using a high-shear turbulent channel flow cell, which included a flow disturbance in the form of a small protrusion. Localized corrosion was observed at the protrusion that could be mitigated with an excess inhibitor concentration. It was found that wall shear stress (up to 5000 Pa) was not the cause of inhibitor failure. The flow acceleration at the leading edge of the protrusion caused a drop in pressure and led to cavitation, with bubble collapse further downstream. This was the main cause of inhibitor failure and localized corrosion. The observed behavior was interpreted in terms of corrosion inhibitor adsorption/desorption kinetics and the associated activation energy analysis.

1. Introduction

Hydrocarbon production and transportation through pipelines and tubing are ubiquitous in the oil and gas industry. Often, water is concurrently produced and transported, containing dissolved corrosive species such as CO₂. Almost all pipelines and much of the tubing are made of mild steel for economic reasons. However, they have a low corrosion resistance to aqueous CO₂ corrosion. Therefore, internal corrosion risk assessment and corrosion inhibition have to be considered to ensure technical integrity over the lifetime of the equipment.

The general mechanisms of uniform CO₂ corrosion in aqueous solutions are well understood, and their description can be found elsewhere [1]. Regarding internal CO₂ corrosion inhibition, use of organic corrosion inhibitors is usually deemed an effective approach [2–8]. These surfactant molecules, when added in very small quantities to the bulk fluid (in the ppm range), form a thin protective film, of the order of nm, on the steel surface by adsorption [9]. The corrosion protection by this inhibitor film relies on its integrity and persistence. Incomplete or otherwise faulty surface coverage by an adsorbed inhibitor film, however, may make the corrosion problem even worse by inducing localized corrosion through establishment of galvanic cells.

The influence of flow on CO₂ corrosion inhibition of mild steel is not fully understood. It is generally accepted that flow affects uninhibited

CO₂ corrosion by enhancing turbulent mass transport of reactive species between bulk solution and the steel surface [10]. The general corrosion rate of the underlying steel increases as the mass transport of corrosive species (e.g., H⁺) from bulk to the steel surface is enhanced [11–15]. Also, fast mass transport of corrosion products (e.g., Fe²⁺) away from the steel surface retards the formation of protective corrosion product layers, e.g., iron carbonate [10,16]. For both of these scenarios, the enhanced mass transport due to turbulent flow makes corrosion more severe. However, there is no coherent evidence of turbulent mass transfer directly affecting the performance of corrosion inhibitors. Actually in many situations, increased turbulent flow resulted in a slight improvement of inhibitor performance [17,18].

It has also been stated that flow may affect protective inhibitor films by hydrodynamic (mechanical) stresses. There is some circumstantial field and laboratory evidence that corrosion inhibitors failed to achieve protection above some “critical” flow velocities, which could be increased by increasing the inhibitor concentration [19–21]. The inhibition failure at these high flow velocities (flow rates) has often been related to high wall shear stress (WSS) which presumably led to removal of the inhibitor film from the steel surface. However, there are also a few detailed studies conducted with high flow velocities that reported that inhibitor performance was not influenced by high WSS [18,22,23]. This begs the question what mechanistic explanation fits

* Corresponding author.

E-mail address: w1234208@ohio.edu (W. Li).

¹ Present address: Center for Applied Energy Research, University of Kentucky, Lexington, KY 40511, USA.

² Present address: State Key Laboratory of Oil and Gas Reservoir Geology and Exploitation, School of Oil and Natural Gas Engineering, Southwest Petroleum University, Chengdu 610500, China.

these seemingly inconsistent open literature data.

Other factors related to flow may also influence corrosion inhibition performance. For example, the presence of solid particles (e.g., sand) in pipe flow is often problematic. Depending on the flow velocity, they may settle at low flow velocities and cause under-deposit corrosion or lead to erosion-corrosion at high velocities [10].

We previously reported on WSS in flow lines but stresses were limited to below 1000 Pa [24]. Moreover, WSS measurements were not accompanied by corrosion rate measurements for inhibited conditions.

In the present study, the effects of high magnitude hydrodynamic stresses on corrosion inhibition in a CO₂ corrosion environment (in the absence of solid particles) were investigated using a thin channel flow cell (TCFC), which generates a highly turbulent disturbed flow with very high local WSS. Corrosion experiments in the presence of an organic inhibitor were performed on a pipeline steel. Electrochemical measurements, weight (mass) loss and surface analysis were utilized to document the observed corrosion. Computational fluid dynamics (CFD) was used as an additional diagnostic tool to characterize the hydrodynamic conditions in the TCFC.

2. Experimental

2.1. Thin channel flow cell

Experiments were performed in a single phase flow loop with a well-defined channel flow test section, which is referred to as: thin channel flow cell (TCFC) due to the high aspect ratio of its cross section. A visual representation for TCFC is shown in Fig. 1. All wetted parts of the flow loop are made of AISI (American Iron and Steel Institute) 316 L stainless steel. A multistage centrifugal pump is employed to achieve the desired flow rate. A liquid tank with a capacity of approximately 150 L is used to prepare and store the test solution. The TCFC test section is 600 mm long, having a rectangular cross-section of 3 mm high and 89 mm wide. The small cross sectional area of the TCFC test section allows the mean flow velocity to reach up to 17 m/s. The mean volumetric flow is measured by a paddlewheel flow meter in a 2.54 cm internal diameter (ID) pipe section downstream of the test section. The temperature of the test section and the liquid tank were constantly monitored by thermocouple probes. The heat generated in the pump was removed by a heat exchanger. In the TCFC test section, four ports spaced along the bottom of the channel are used to flush-mount plug-in probes such as a differential pressure transducer, wall shear stress measurement probe [24], electrochemical corrosion probe, and weight loss corrosion specimen.

2.2. Corrosion specimens

Three different weight loss corrosion specimens and an electrochemical corrosion probe were used to measure corrosion. For the weight loss specimens, two simple cylindrical specimens and a special cylindrical specimen with a protrusion on its top surface were used. These specimens were all made of API (American Petroleum Institute) 5L X65 mild steel (chemical analysis [wt.%]: 0.05C, 1.51 Mn, 0.03 Nb, 0.004 P, 0.001 S, 0.01 Ti, 0.04 V, the balance being Fe) and were numbered as Specimen 1, Specimen 2 and Specimen 3 with respect to flow direction. Specimen 1 and Specimen 2 had a cylindrical shape with a diameter of 3.18 cm and 0.64 cm in height (as shown in Fig. 2). Specimen 1 was sequentially ground with 400 and 600 grit SiC sand papers, while Specimen 2 was ground with 150 grit SiC sand paper, aiming to investigate the effect of initial surface roughness on corrosion inhibition. Except for the top surface, which was flush to the bottom plate of the TCFC and exposed to the corrosion environment, all other surfaces of the specimens were coated with corrosion resistant paint.

Specimen 3 with a protrusion was sequentially ground with 400 and 600 grit SiC sand papers. The specification and orientation of Specimen 3 with respect to flow direction are shown in Fig. 3. This specimen had a trapezoidal-prism-shaped protrusion on top of the cylindrical base. While the cylindrical base was flush to the bottom plate of the flow cell, the trapezoidal prism protruded out of the bottom plate into the flow cell, similar as a weld bead may do in a real pipeline. The protrusion was expected to significantly change the local hydrodynamic conditions, leading to a much higher local WSS, and affect the inhibitor film on the metal surface. Other than the top surface of Specimen 3 that was exposed to flow and corrosion, all other surfaces were coated with corrosion resistant paint. On the top surface of Specimen 3 one can identify 5 distinct regions, which are supposed to experience very different flow conditions, as shown in Fig. 3. They were termed: 1 = upstream flat; 2 = upstream slope; 3 = top of protrusion; 4 = downstream slope; 5 = downstream flat.

A three-electrode cylindrical electrochemical probe was employed for online electrochemical measurements during the experiments. As shown in Fig. 4, the ring shaped working electrode made of the same X65 mild steel has a surface area of 0.85 cm². The outer body of the electrochemical probe, which is made of 316L stainless steel, was used as the counter electrode. The surface of the electrochemical probe was ground with 400 grit and 600 grit SiC sand papers sequentially prior to experiments. A saturated Ag/AgCl reference electrode was installed in the downstream section of the TCFC test section, to provide a stable and accurate potential reading for electrochemical measurements. Before each experiment, the reference electrode was checked with a standard saturated calomel electrode to ensure consistency of the potential

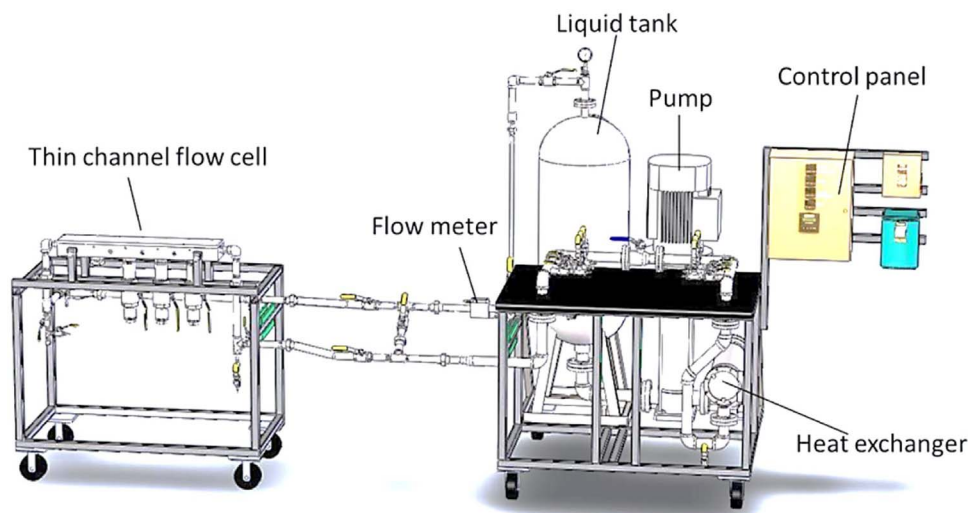


Fig. 1. Visual representation of the thin channel flow cell assembly.

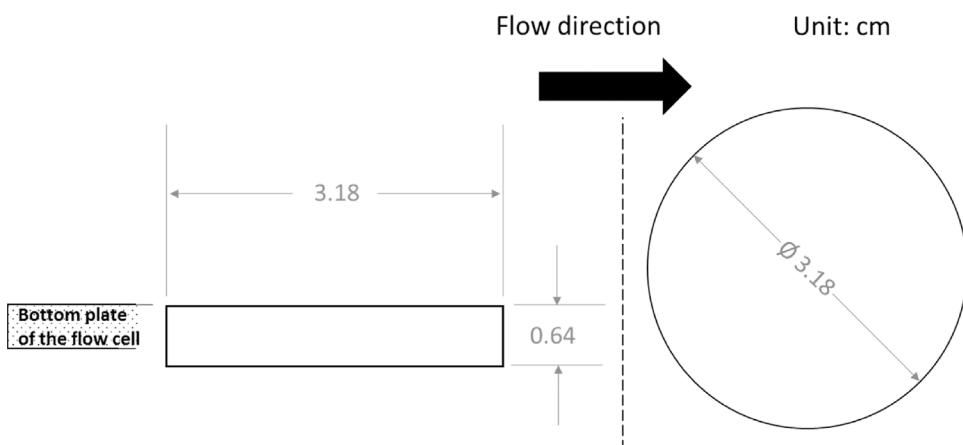


Fig. 2. Specification and flow orientation of flat weight loss specimens. Left: side view; right: top view.

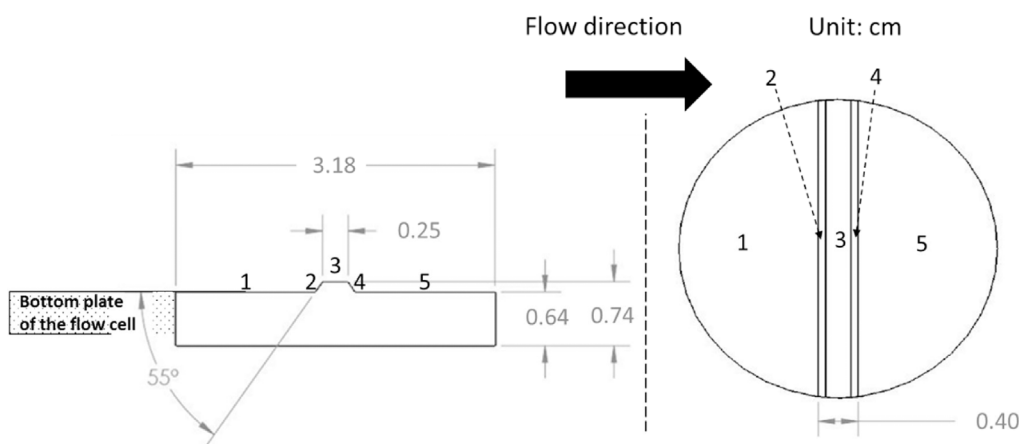


Fig. 3. Specification and flow orientation of protrusion weight loss specimen (left: side view; right: top view). Distinct geometrical regions of the surface are marked by numbers 1–5.

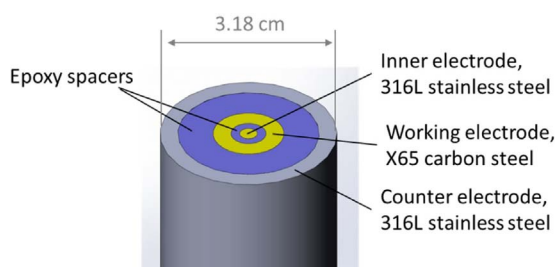


Fig. 4. Configuration of the electrodes in the electrochemical probe.

reading.

The three weight loss specimens and the electrochemical probe were flush-mounted to the bottom plate in the TCFC test section in a sequence as shown in Fig. 5. All weight loss specimens were fixed in position by using a mechanical specimen holder underneath (as shown in Fig. 5). The protrusion specimen (Specimen 3) was placed furthest downstream (port 4) to minimize the flow disturbance to other specimens.

2.3. Experimental procedures

The test matrix for this series of experiments is shown in Table 1. All experiments were conducted at 25 °C, 0.97 bar CO₂ partial pressure and a pH value of 5.0, set to achieve a low FeCO₃ saturation value ($S_{\text{FeCO}_3} < < 1$) [16,25]. Accordingly, no FeCO₃ layer formation was expected, nor was such layer visually observed on the specimen surfaces in any of the following experiments, which was confirmed by surface analysis.

Preparation for each experiment was done using the following

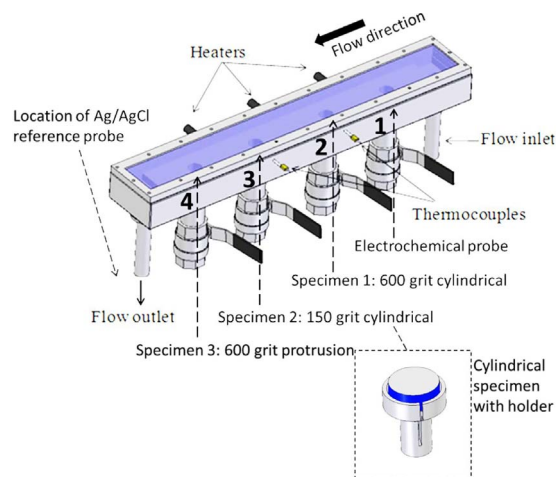


Fig. 5. Location arrangement of the specimens in the TCFC test section.

procedure. A 1 wt.% sodium chloride (NaCl) aqueous solution, 132 L in volume, was prepared with deionized (DI) water in the liquid tank of the TCFC system, purged with a continuous CO₂ gas flow, and maintained at the test temperature of 25 °C. The O₂ level of the system was monitored by an electrochemical O₂ sensor located at the purging outlet of the tank. The pressure in the tank for all experiments was maintained at atmospheric pressure; the CO₂ partial pressure was 0.97 bar, the balance made by the water vapor pressure being 0.03 bar at this temperature. The solution pH was adjusted to the required value by addition of sodium bicarbonate (NaHCO₃), and was constantly monitored by an immersed pH probe. After polishing, all mild steel specimens were cleaned in an ultrasonic bath with isopropanol ([CH₃]₂CHOH),

Table 1
Test matrix for corrosion inhibition experiments.

Corrosion specimen material	X65 mild steel
Temperature	25 ± 2 °C
Total pressure	1.0 bar at the holding tank ~7.0 bar at the test section inlet
Liquid phase	1 wt.% NaCl aqueous solution
Gas phase	0.97 bar CO ₂
Test pH	5.0 ± 0.2
Flow velocity	16 m/s
Test duration	4 days
Inhibitor concentration	0, 72, 720 ppm _v
Dissolved O ₂ concentration	O ₂ < 30 ppb, O ₂ < 2 ppb

Note: ppm_v: part per million (10⁻⁶), by volume; ppb: part per billion (10⁻⁹), by weight.

dried by nitrogen gas and weighed to the nearest tenth of a milligram. Surface analysis was conducted on each of the specimens prior to the experiments. The surface morphology was characterized by scanning electron microscopy (SEM), Energy-dispersive X-ray spectroscopy (EDS) and profilometry. After surface analysis, all specimens were rinsed with isopropanol and flush-mounted to the bottom plate of the isolated TCFC test section. The test section was then deaerated with dry CO₂ gas. Finally, the prepared test solution in the liquid tank was diverted to the test section so that the specimens were immediately exposed to the solution with a designated flow velocity, pH, CO₂ concentration and temperature.

During each experiment, a potentiostat connected with the electrochemical corrosion probe was used for performing electrochemical measurements. The open-circuit potential (OCP) was continuously monitored, and linear polarization resistance (LPR) measurements were conducted systematically to provide in situ corrosion rate measurements. The potential polarization range was ± 5 mV versus OCP with a scanning rate of 0.1 mV/s. The solution resistance was measured with electrochemical impedance spectroscopy (EIS) in order to compensate the measured polarization resistance.

A deaerated aqueous solution containing the corrosion inhibitor was added to the system typically 10–12 h after the beginning of the experiment when the corrosion rate was stable and the surface of the mild steel specimen was pre-corroded. Each experiment typically lasted another 4 days, following the addition of inhibitor. In this work, a surfactant-type inhibitor package was used, containing analytical grade chemicals: tall oil fatty acid diethylenetriamine (TOFA/DETA) imidazolium salt (24 wt.% TOFA/DETA imidazolium, 10 wt.% acetic acid, 13 wt.% 2-Butoxyethanol, and the balance being water). The molecular structure of TOFA/DETA imidazolium is depicted in Fig. 6, which contains a hydrophobic hydrocarbon tail and a hydrophilic head group [26]. The adsorption of this molecule is presumably driven by electrostatic interactions between the charged head group (the five-membered nitrogen ring) and the oppositely charged steel surface [27]. In addition, the pendant side chain may provide a secondary site for inhibitor adsorption [28]. When present in a high enough concentration,

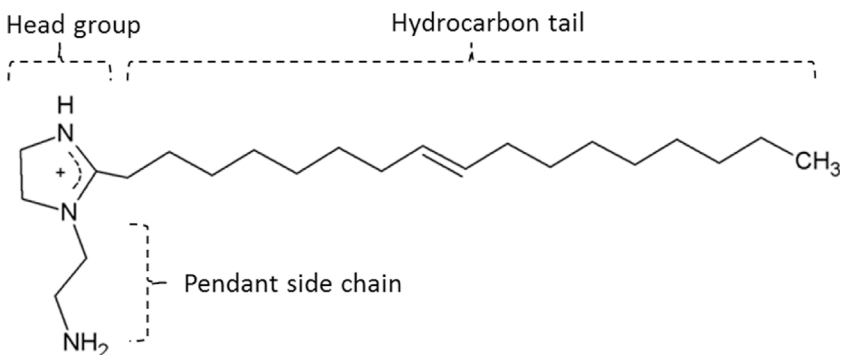


Fig. 6. Molecular structure of TOFA/DETA imidazolium.

these inhibitor molecules form an adsorbed protective film on the steel surface and effectively reduce the corrosion rate. A typical inhibitor package concentration of 72 ppm_v was used in the experiments, which exceeds the reported critical micelle concentration (CMC) value for this inhibitor package (36 ppm_v) [17,29], and should effectively mitigate the corrosion at the tested temperature and pH [30]. The results reported below are based on the inhibitor package concentration.

After each corrosion experiment, all weight loss specimens were carefully taken out of the TCFC, immediately immersed into deaerated deionized water to remove soluble salts and impurities on the specimen surface and then dehydrated by using isopropanol. Then, the specimens were cleaned in an ultrasonic bath with isopropanol, dried by nitrogen gas, weighed to the nearest tenth of a milligram, and stored in a vacuum desiccator for further post-test surface analyses.

2.4. Computational fluid dynamics

In this study, computational fluid dynamics (CFD) simulation of the flow in the TCFC test section was performed, using ANSYS FLUENT Academic Research R 14.0 and R 15.0. The CFD simulation results allowed for estimations of local hydrodynamic parameters at the corroding specimens, which are not easy to obtain by experimental means.

A simulation geometry was constructed based on the inner dimensions of the TCFC test section; a tetrahedral computational mesh was generated. The standard *k-ε* turbulent model was used with an enhanced wall treatment. A uniform velocity-inlet boundary condition was selected (16 m/s) and a pressure-outlet boundary condition was set with a gauge pressure of zero. A symmetry boundary condition was applied at the length-wise symmetry plane of the TCFC test section, to save computational resources. Wall functions with a no slip wall boundary condition were applied to all other solid walls. For solution of the equations, the SIMPLE scheme was chosen for pressure-velocity coupling. For spatial discretization, second order upwind scheme was used for momentum, turbulent kinetic energy and turbulent dissipation rate. The simulation was considered converged when the normalized residuals of all equations were stable and below 5 × 10⁻⁴.

3. Results

3.1. Corrosion experiments without inhibitor

A “blank” test without addition of corrosion inhibitor was conducted first, and the corrosion rates were measured by weight loss and LPR. The time averaged mass losses from all three corrosion specimens were measured and the average uniform corrosion rate was calculated to be 5.7 ± 0.7 mm/yr. The time evolution of the uniform corrosion rate was also monitored (at sampling interval of 1 or 2 h) by using the LPR technique, which measures the polarization resistance (*R_p*) of the working electrode and calculates the corrosion current (*I_{corr}*) via the Stern-Geary equation [31]:

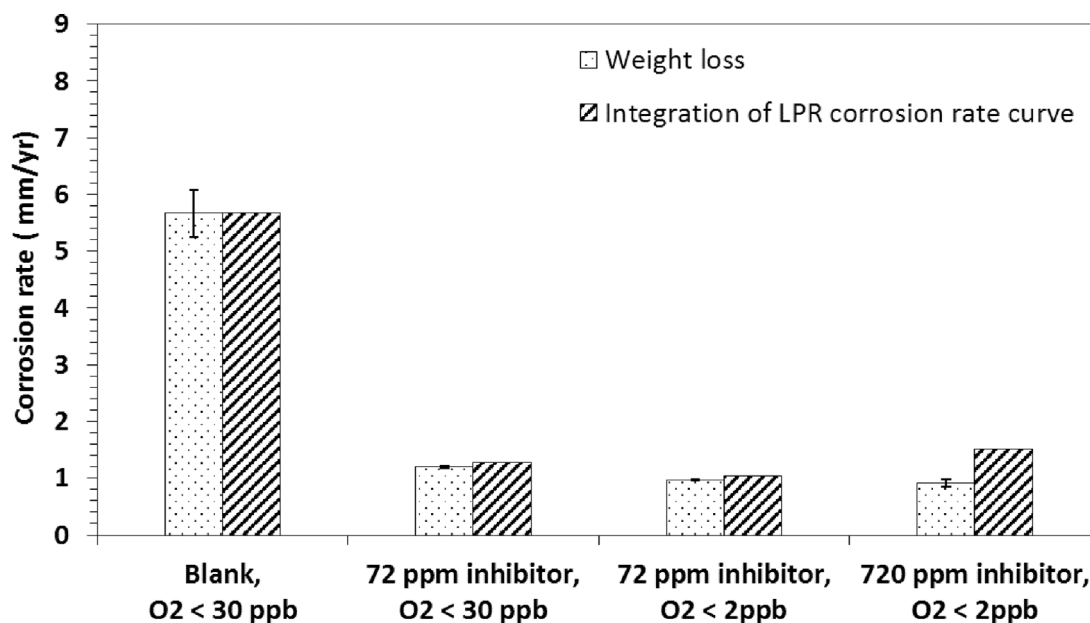


Fig. 7. Corrosion rates calculated from the time averaged weight (mass) loss, compared to the integrated LPR corrosion rates using $B = 65$ mV. Other conditions: 1 wt.% NaCl aqueous solution, pH 5, $p\text{CO}_2 = 0.97$ bar, 25 °C, 16 m/s, 4 day test duration, X65 steel.

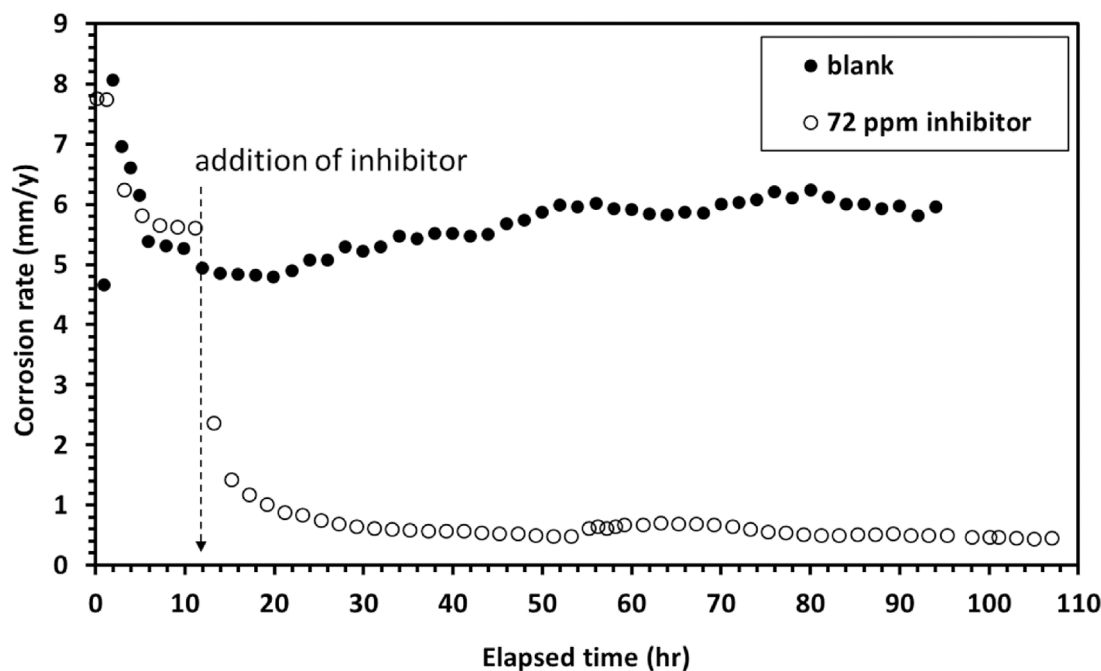


Fig. 8. LPR corrosion rates for blank test and for a 72 ppm, imidazolinium inhibitor test. Other conditions: 1 wt.% NaCl aqueous solution, pH 5, $p\text{CO}_2 = 0.97$ bar, 25 °C, 16 m/s, 4 day test duration, X65 steel, $\text{O}_2 < 30$ ppb.

$$I_{corr} = \frac{B}{R_p} \quad (1)$$

where B is the proportionality constant (V), also known as the “ B value”. The corrosion current was used to calculate the rate of uniform metal loss due to the corrosion from Faraday’s law of electrolysis [31]. For corrosion of mild steel (which is mostly iron), when all the physical properties are substituted, the calculated corrosion current is related to the corrosion rate, as:

$$r_{corr} = 1.16 \cdot \frac{I_{corr}}{S} \quad (2)$$

where r_{corr} is the corrosion rate (mm/yr); I_{corr} is the corrosion current (A); and S is the surface area of the electrode (m^2).

It should be noted that the B value, required to calculate the corrosion rate from the LPR, is not known a priori. The B value can theoretically be obtained from the Tafel slopes, which can be determined, for example, from potentiodynamic sweeps. The sweeps need to be conducted over a wide enough potential range (typically 0.3–0.5 V below and above the open circuit potential) to get the required current range, spreading over at least two decades. While one is looking for straight portions of the polarization curves in the charge transfer controlled regions to determine the Tafel slopes, this is not always straightforward. Due to the presence of limiting currents on the cathodic side and (pre)passivation on the anodic side, one often cannot find any “straight enough” portions of the curves and the identification of Tafel slopes becomes difficult. Furthermore, the large overpotentials

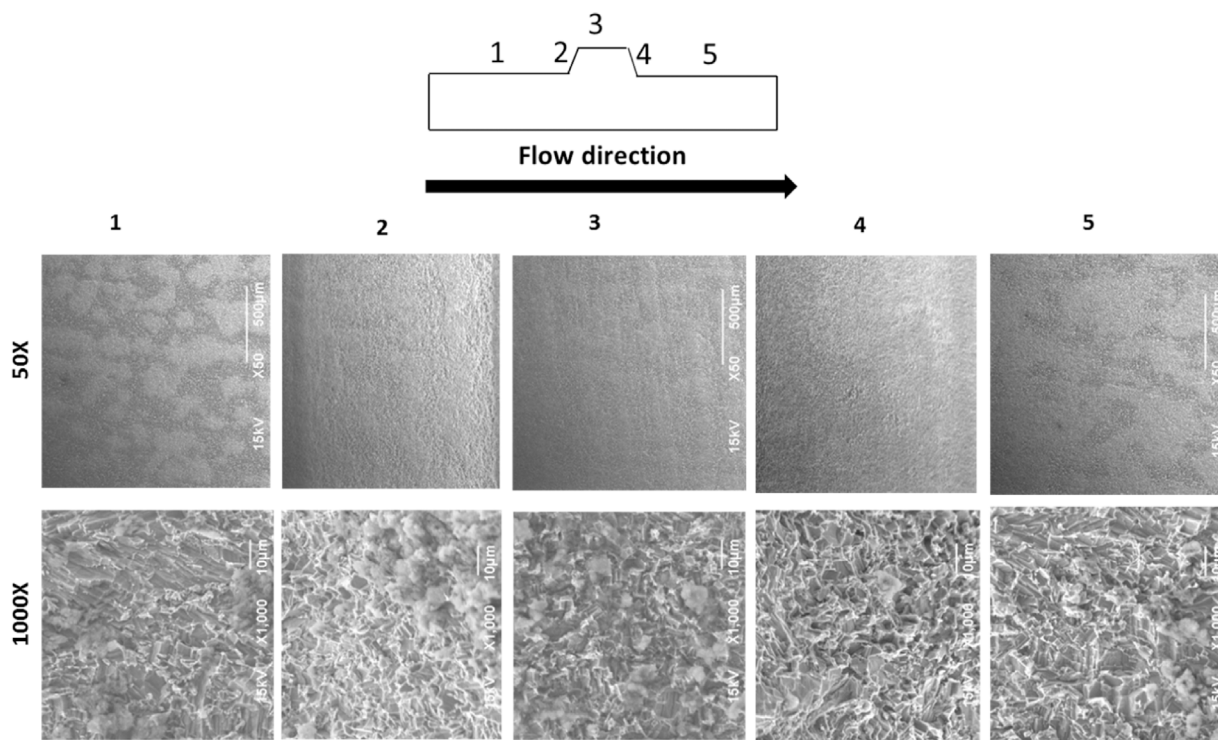


Fig. 9. SEM images of the protrusion Specimen 3 after the blank test (no inhibitor). 1st row: 50X magnification; 2nd row: 1000X magnification. Conditions: 1 wt.% NaCl aqueous solution, pH 5, $p\text{CO}_2 = 0.97$ bar, 25 °C, 16 m/s, 4 day test duration, X65 steel, $\text{O}_2 < 30$ ppb.

that need to be applied during such polarization can drastically alter the water chemistry at the electrode surface and even change the nature of the surface under investigation. Even if this is acceptable, it is usually considered best practice to do the potentiodynamic sweeps only at the end of long experiments, in order to minimize the disruption. However, this only provides a single data point on Tafel slopes and one has to assume that the same corrosion mechanisms and Tafel slopes were valid throughout the experiment. Another option is to adopt Tafel slopes from mechanistic studies of cathodic and anodic processes underlying corrosion.

In the current case, from potentiodynamic sweeps it was found that the corrosion current was close to the cathodic limiting current, and that the corresponding anodic Tafel slope was approximately 120 mV/decade, values that have been reported in previous mechanistic studies of CO_2 corrosion [1,32]. This leads to a B value of 52 mV, and given that the time-averaged polarization resistance obtained from LPR measurements (compensated for solution resistance) was 156 ohm, one gets a corrosion rate of approximately 4.5 mm/yr. This is lower than the 5.7 mm/yr determined by weight loss. However, given all the uncertainties with determining the B value listed above, this discrepancy is not surprising and can be accepted for the purposes of the present study, which is focused predominantly on occurrence of localized attack.

For a lack of having a more accurate estimate, the B value was taken to be 65 mV, in order to match the averaged weight loss measurements in the experiment without the inhibitor, and was then used for calculation of corrosion rates in different series of experiments, both with and without the inhibitor. This implies an assumption that the same corrosion mechanisms (Tafel slopes) are valid across the different conditions covered in this study. To justify the use of B value of 65 mV, the corrosion rates calculated from time-averaged polarization resistance (LPR) measurements were compared with those obtained from weight (mass) loss series of experiments, for all experiments done both with and without the inhibitor, as shown in Fig. 7. The generally coherent corrosion rates obtained by the two methods suggest that this B value was suitable for the present experiments conducted at very high

flow velocities.

It should be stressed that the dissolved O_2 concentration was carefully monitored during the whole experiment to detect and avoid the possible interference with corrosion measurements, particularly at high velocities. The highest value recorded in this first series of experiments was 30 ppb while the lowest value was 4 ppb. Because of this, the concentration of dissolved O_2 in this experiment was denoted hereafter as being < 30 ppb. Experimental results with a more strict dissolved O_2 control are shown below.

The corrosion rate evolution for the blank test, obtained from LPR measurements, is shown in Fig. 8. The mild steel surface morphologies of all the weight loss specimens were examined by SEM and EDS. For example, Fig. 9 shows the surface details of the protrusion specimen obtained by SEM, using the same numeration for the distinct regions described earlier in Fig. 3. The surface analysis indicates that uniform corrosion occurred on the protrusion specimen across the different regions. The surface morphologies for the flat specimens showed a very similar pattern as that seen for the protrusion specimen and are therefore not shown here. The elemental composition of the specimen surface after the experiment was analyzed by EDS; a similar result was observed for all the weight loss specimens, as exemplified by Fig. 10. When comparing these results with those obtained on a FeCO_3 covered steel surface [16], it is concluded that no formation of FeCO_3 layers occurred in the blank test.

3.2. Corrosion experiments with inhibitor

To investigate the effect of high turbulent flow on inhibitor performance, the TOFA/DETA imidazolium chloride inhibitor was used at a concentration of 72 ppm_v while other test parameters remained unchanged. The steel specimens were precorroded for approximately 10–12 h before the addition of inhibitor. Fig. 8 shows the uniform corrosion rates during the experiment with a direct comparison to those of the blank test. It clearly shows that, after the addition of inhibitor, the general corrosion rate “immediately” halved and then gradually decreased to 0.4 mm/yr. The corrosion inhibitor effectively retarded

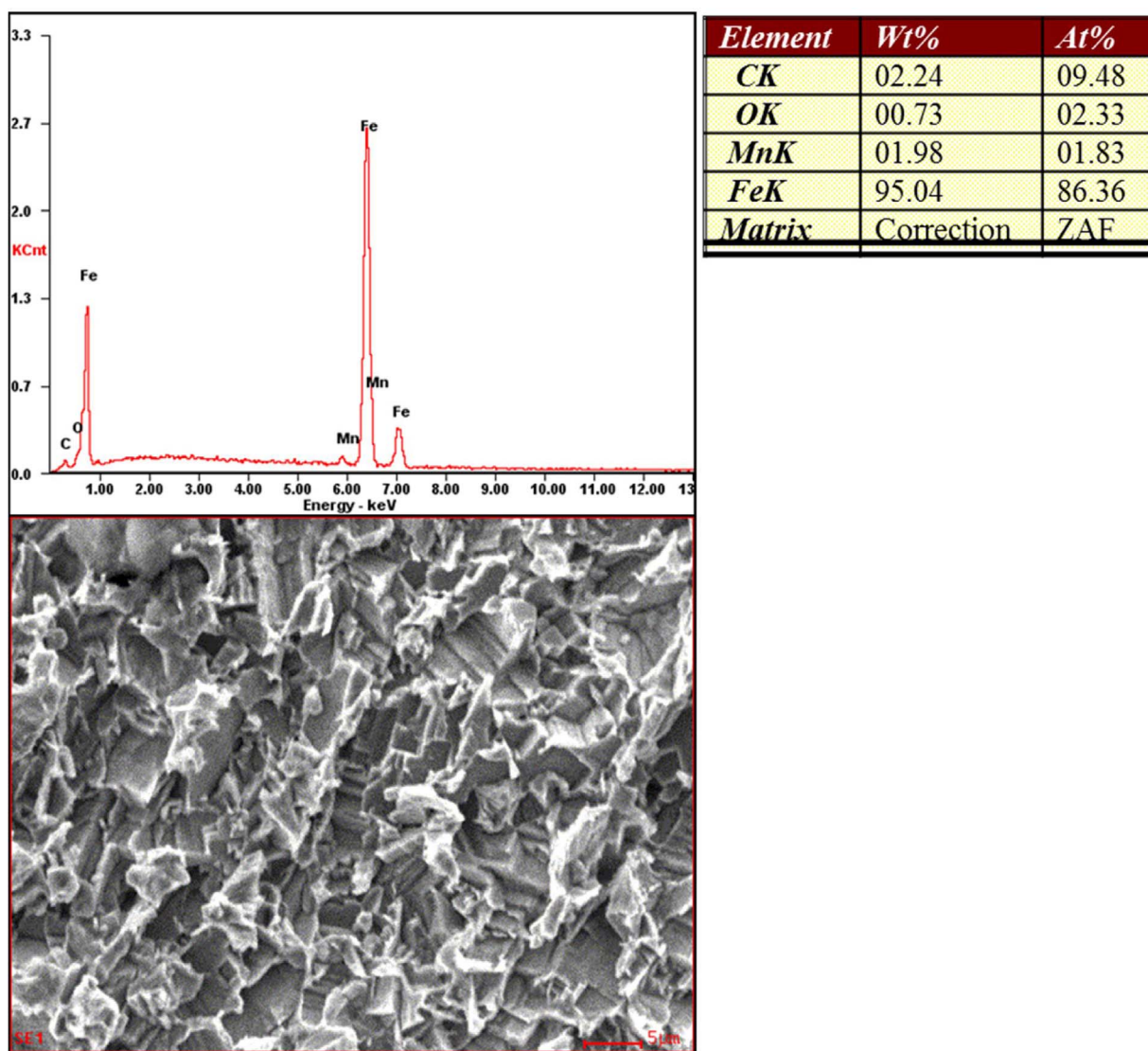


Fig. 10. EDS analysis of the flat Specimen 2 after the blank test (no inhibitor). Conditions: 1 wt.% NaCl aqueous solution, pH 5, $p\text{CO}_2=0.97$ bar, 25 °C, 16 m/s, 4 day test duration, X65 steel, $\text{O}_2 < 30$ ppb.

the general corrosion rate by almost 95%, even in the presence of such a high flow velocity (16 m/s). A comparison of the surface morphologies of the specimens after the experiments shows a distinct difference between the blank test and the inhibitor test.

The surface morphologies of all weight loss specimens from the inhibition test are shown in Fig. 11 and Fig. 12. For flat specimens with a varied initial surface roughness, the final surfaces are quite similar. They are also similar to those obtained in the blank test without inhibitor (see Fig. 9); a uniformly corroded surface can be observed, presumably due to the pre-corrosion step. But severe pitting corrosion was found in middle section of region 3 (top) of the protrusion specimen after the experiment, as shown in Fig. 12. Some much smaller pits are also seen at the leading edge between region 2 and 3. The depths of the observed pits were evaluated by surface profilometry. Fig. 13 shows the surface profile for the affected region on the top of the protrusion. One of the deepest pits was found to be 140 μm deeper than the surrounding area (Fig. 13B), which is equivalent to a time averaged pit penetration rate of 11.4 mm/yr. It is noted that this pit penetration rate in the presence of inhibitor is about 30 times higher than the average corrosion rate of the inhibited surface around it. Interestingly, the pit penetration rate is also much higher than the uniform corrosion rate of the blank test without any inhibitor (5.7 mm/yr), which suggests that a galvanic cell probably developed between the fast corroding pit

and the protected surrounding surface. However, no pitting was observed in regions 1, 4 and 5, which generally showed a uniformly corroded surface similar to that of the flat specimens. The chemical composition of all specimens after the experiment was analyzed by EDS, which showed similar results – a corroded steel surface without any corrosion products.

In summary, the experiment with 72 ppm_v inhibitor demonstrated that the TOFA imidazolium chloride inhibitor effectively retarded the general corrosion rate even at this high flow velocity (16 m/s). However, for areas of disturbed flow due to a sudden flow geometry change, as seen at the protrusion, severe localized corrosion occurred. These results were repeated three times and at that stage it was unclear why localized corrosion occurred. It was also not clear why the localized attack was most severe at the top of the protrusion region away from the leading edge. Was it because of the higher velocity, turbulence, wall shear stress, or some other unidentified reasons? Further analysis was needed as described in the following sections.

3.3. Effect of dissolved oxygen on corrosion inhibition

One of the first concerns was that the localized attack described above was somehow created as an artifact of the experimental setup, procedures or conditions. For example, it has been reported that O_2

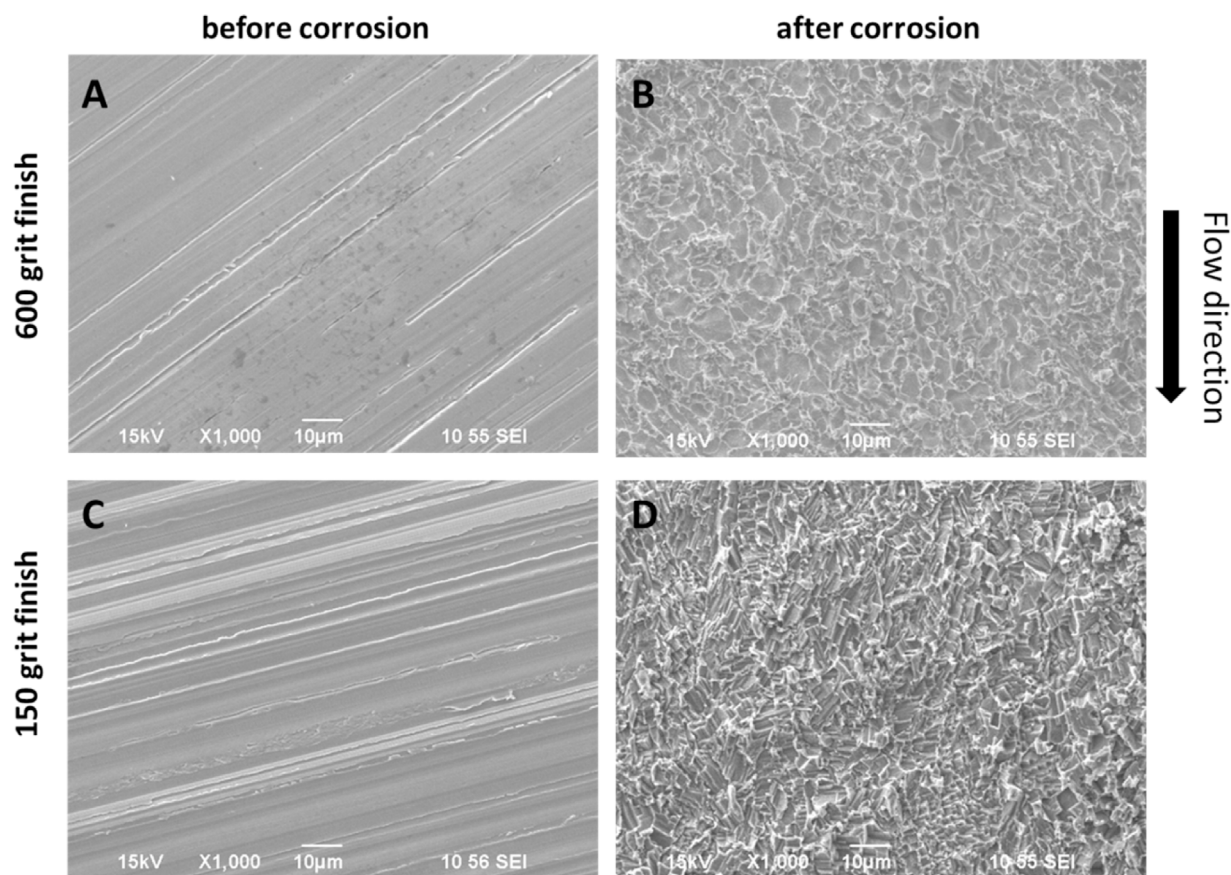


Fig. 11. SEM images before and after experiment at 1000X magnification. 1st row: flat Specimen 1 at 600 grit finish and 2nd row: flat Specimen 2 at 150 grit finish. Conditions: 72 ppm_v inhibitor, 1 wt.% NaCl aqueous solution, pH 5, pCO₂=0.97 bar, 25 °C, 16 m/s, 4 day test duration, X65 steel, O₂ < 30 ppb.

ingress can significantly increase corrosion rate for a corrosion inhibition system. Generally, corrosion inhibitors for CO₂ corrosion do not work well with oxygen. For example, Gulbrandsen et al. suggested that dissolved O₂ may penetrate the adsorbed corrosion inhibitor films to reach the steel surface, and this process is accelerated by turbulent flow due to the enhanced mass transfer [12]. However, any effect of dissolved O₂ on localized corrosion in the presence of inhibitor was not mentioned. Therefore, in the present study, it was first suspected that the localized corrosion observed on the top of the protrusion specimen was somehow related to the small and undesired presence of dissolved O₂ in the experiments.

Consequently, the 72 ppm_v inhibitor experiment was repeated with the O₂ level maintained at a very low level – below 2 ppb (denoted hereafter as < 2 ppb) by continuously purging the solution in the holding tank with an ultra-high purity CO₂ gas (99.999%). Fig. 14 shows the comparison of corrosion rates between the two experiments with different levels of dissolved oxygen. It shows that the general corrosion was well inhibited in both experiments. The experiment with lower dissolved O₂ content had a slightly lower final corrosion rate after the addition of inhibitor, which is consistent with the observations by Gulbrandsen et al. [22].

The surface analysis for flat specimens revealed that only uniform corrosion occurred, similar to previous experiments; and it is therefore not shown here. The surface morphology of the protrusion specimen before and after this experiment is shown in Fig. 15. Once again, some minor pitting corrosion was found close to the leading edge and much more was further downstream – on the top of the protrusion region. Fig. 16 shows the surface depth profile at the top of the protrusion region obtained by profilometry. One of the deepest pits was found to be 154 µm below the surrounding area, which is equivalent to a pit penetration rate of 12.5 mm/yr.

Comparison of the results obtained with very low dissolved O₂ concentration (less than 2 ppb O₂) with those done at somewhat higher dissolved O₂ concentration (up to 30 ppb O₂), revealed that the locations of the pits and the magnitude of the localized attack were similar. It was therefore concluded that the severe localized corrosion found on the top surface of the protrusion specimen was not caused by small amounts of dissolved O₂. Other possible causes were sought to explain the experimental results.

3.4. Effect of wall shear stress on corrosion inhibition

After eliminating the dissolved O₂ as the cause for the observed localized attack, the next hypothesis tested was the much debated effect of the WSS. It appeared plausible that the disturbed flow, caused by the sudden flow geometry change near the protrusion, significantly altered the local hydrodynamic conditions [33], leading to a higher magnitude of local WSS and causing local removal of inhibitor from the steel surface. Barring very complicated and expensive hydrodynamic measurements, CFD simulation was deemed a suitable diagnostic tool to analyze the hydrodynamic conditions around the protrusion specimen. The actual flow geometry of the main part of the TCFC test section was reconstructed using ANSYS FLUENT, with the attention focused on the protrusion specimen (as seen in Fig. 17). The length-wise symmetry plane is outlined by red lines, which is perpendicular to the bottom plate of the TCFC and parallel to the flow direction.

The detailed simulation setup was described earlier in section 2.4. Hydrodynamic parameters such as flow velocity, WSS, kinetic energy of turbulence and static pressure were calculated for the entire domain. Fig. 18 shows the 2-D flow velocity profile field across the length-wise symmetry plane. It clearly demonstrates that the protrusion significantly changes the local flow velocity field. The highest flow

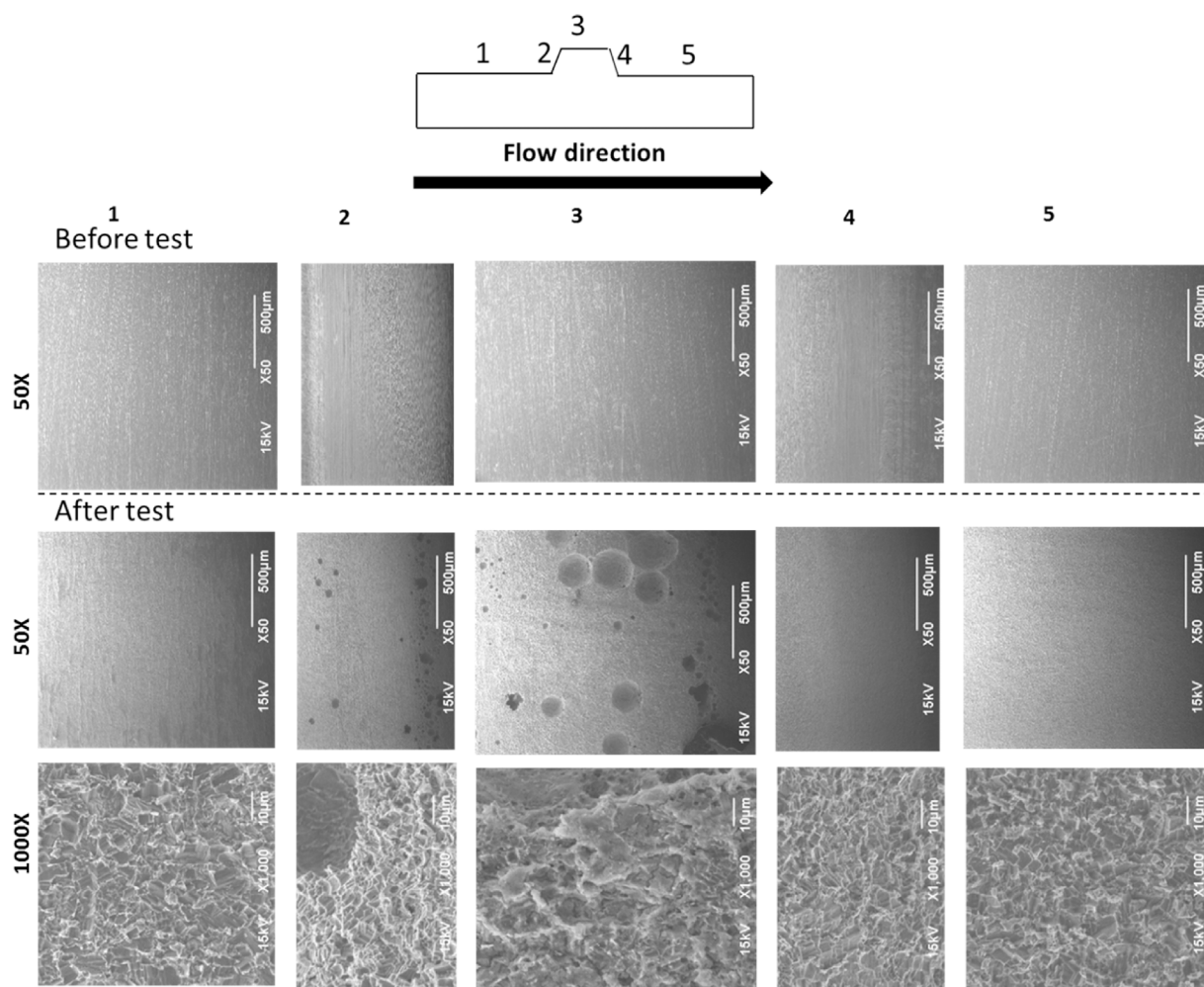


Fig. 12. SEM images of the protrusion Specimen 3. Before test: 1st row at 50X magnification. After test: 2nd row at 50X magnification and 3rd row at 1000X magnification. Conditions: 72 ppm_v inhibitor, 1 wt.% NaCl aqueous solution, pH 5, pCO₂=0.97 bar, 25 °C, 16 m/s, 4 day test duration, X65 steel, O₂ < 30 ppb.

velocity (28 m/s) occurs near the leading edge where the upstream slope and the top surface of the protrusion meet. The corresponding 3-D field of the WSS in the vicinity of the protrusion is shown in Fig. 19. In addition, the 2-D WSS distribution across the symmetric plane is shown in Fig. 20A, with the magnitude of WSS at the bottom of the symmetric plane plotted in Fig. 20B.

It can be seen that the upstream and downstream regions away from the protrusion have an average WSS of 500–800 Pa, which is consistent with the results from direct WSS measurements by a floating element sensor at the same flow conditions [24]. A sudden increase of WSS occurs on the leading edge of the protrusion specimen. A maximum WSS value in the range of 4600–4900 Pa is calculated there, which then rapidly decreases moving further downstream along the top surface of the protrusion. By the middle section of the top surface of the protrusion, where most of the deep pits were found, the WSS value is in the range of 1900–2300 Pa. If WSS was the cause for the localized inhibitor removal and localized attack, the most severe pitting should have been found at the leading edge of the protrusion, which clearly was not the case, as shown in the micrographs above. A similar conclusion was reached when analyzing the field of near-wall kinetic energy of turbulence (describing the intensity of turbulent fluctuations), which also peaks at the leading edge of the protrusion (as shown in Fig. 21). In addition, the WSS required to remove this type of inhibitor from a steel surface is expected to be at least 10⁶ Pa or greater [24], which is several orders of magnitude larger than the calculated maximum WSS values. Therefore, it is unlikely that local WSS was the cause of the observed inhibitor failure and pitting corrosion. The search for alternative

explanation continued, and after a lot of analysis – cavitation became the focus, as described in the section below.

3.5. Effect of cavitation on corrosion inhibition

Because of the sudden increase of flow velocity at the leading edge of the protrusion (see Fig. 18), the pressure at this location is greatly reduced, which follows from Bernoulli's principle [34]. The total pressure distribution across the symmetry plane is shown in Fig. 22, which clearly illustrates the sudden drop of pressure at the leading edge of the protrusion forming a zone where the total absolute pressure approaches zero, as indicated by the CFD simulation. In reality, it is expected that the pressure at that location reached as a minimum the water vapor saturation pressure (0.032 bara at 25 °C), and vapor bubbles formed. The formation of condensable water vapor bubbles is often considered to be “instantaneous” given the thermodynamically favorable conditions, since it is much faster than most other associated processes of momentum, heat and mass transfer. In reality, the process of bubble nucleation is of the order of μs [35]. This suggests that, for the current case, the residence time of the water in the low pressure region at the leading edge was sufficient to enable bubble formation. From Fig. 22 it can also be seen that the pressure along the top wall of the protrusion quickly recovers and reaches 1.8 bara somewhere around the middle of protrusion where localized attack was observed. Given the local flow velocities, the time it took for the bubbles to reach the middle of the protrusion is of the order 100 μs, which is a typical time required for the vapor bubbles to collapse when exposed to high pressure [36–38].

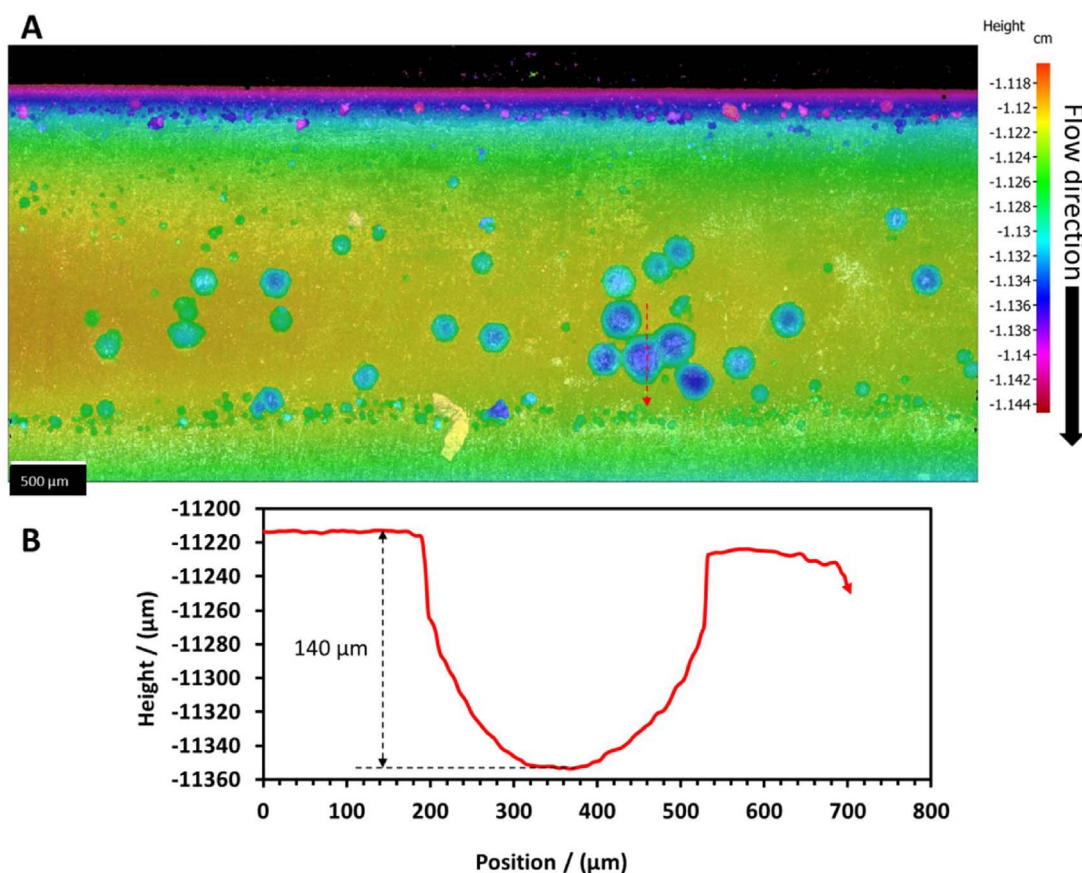


Fig. 13. (A): Profilometry image after the experiment of the surface on the top of the protrusion Specimen 3; (B): depth scan across the dotted red line marked in (A). Conditions: 72 ppm_v inhibitor, 1 wt.% NaCl aqueous solution, pH 5, pCO₂=0.97 bar, 25 °C, 16 m/s, 4 day test duration, X65 steel, O₂ < 30 ppb. (For interpretation of the references to color in this figure legend, the reader is referred to the web version of this article.)

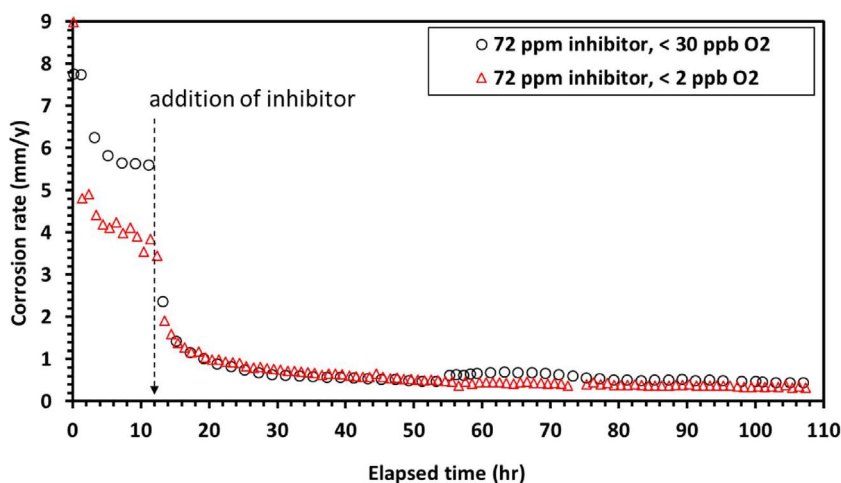


Fig. 14. LPR corrosion rates for experiments with varied levels of dissolved O₂ concentration. Conditions: 72 ppm_v inhibitor, 1 wt.% NaCl aqueous solution, pH 5, pCO₂=0.97 bar, 25 °C, 16 m/s, 4 day test duration, X65 steel.

The collapsing bubbles would have generated shock waves in the vicinity of the steel surface, which rapidly reached the surface, thereby imposing large mechanical stresses that could locally remove inhibitors and induced localized corrosion. Calculations found in the open literature indicate that mechanical stresses of the order of 10^8 – 10^9 Pa are possible due to implosions of cavitation bubbles [39–41], which exceed the required forces to remove inhibitor films from a steel substrate that of the order of 10^6 – 10^7 Pa [42]. This seems to be a plausible explanation that fits the experimental findings.

In order to verify the cavitation mechanism derived from CFD results and experimental evidence, an additional corrosion experiment was carried out. The idea was to eliminate the hydrodynamic

conditions that lead to cavitation without changing other conditions. Consequently, localized corrosion would not be expected if cavitation was the true cause. For all previous experiments, the protrusion specimen was located at the furthest downstream port (port 4), shown in Fig. 5. The measured pressure drop between port 1 and port 4 was 1.2 bar at the flow velocity of 16 m/s. Hence, by moving the protrusion specimen to port 1 (furthest upstream), the calculated absolute pressure at the protrusion should be much higher than the water vapor pressure at this temperature. Therefore, neither cavitation nor localized corrosion would be expected.

In this additional corrosion experiment, except for the change of the location for the protrusion specimen in the TCFC, all other experimental

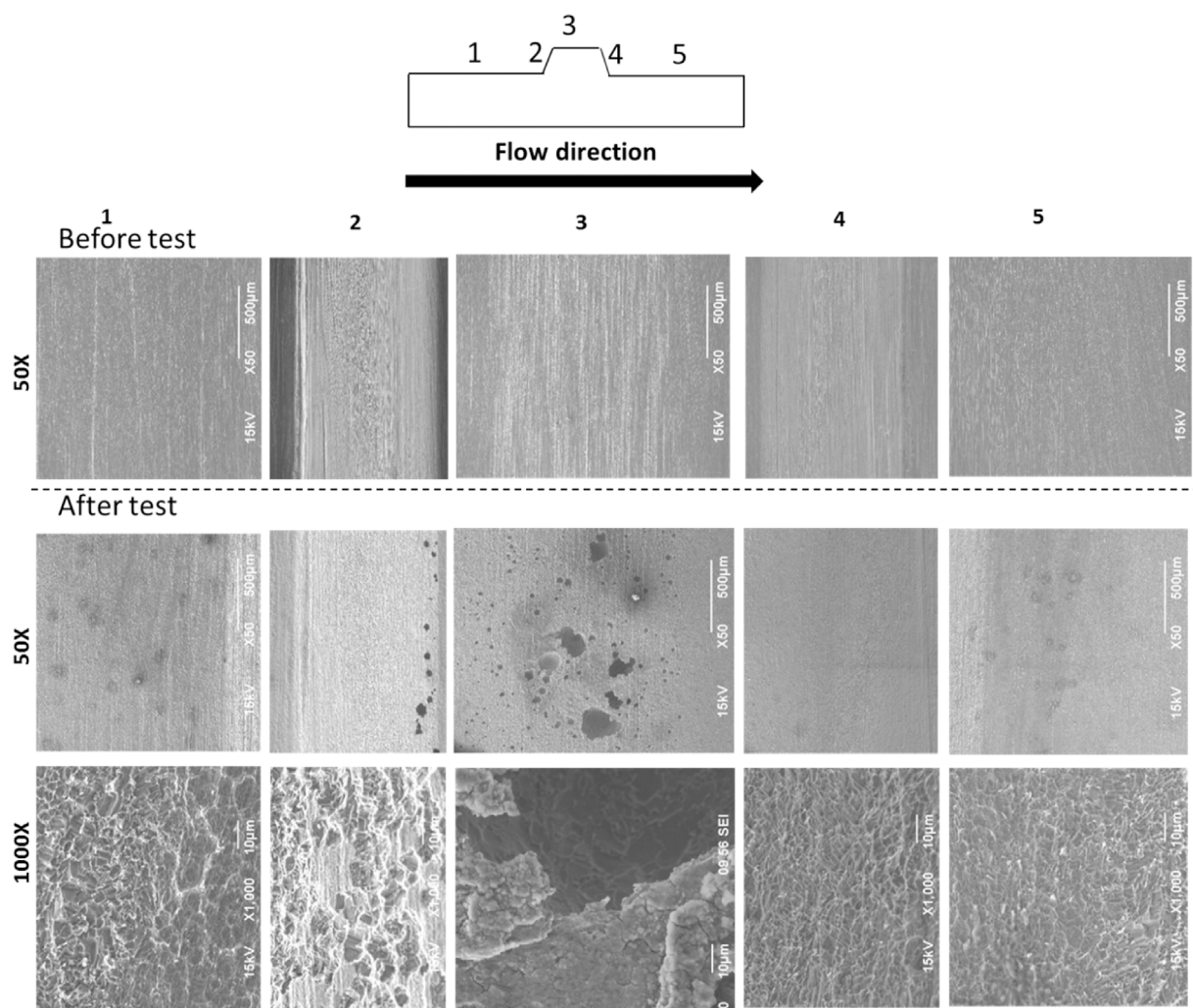


Fig. 15. SEM images of the protrusion Specimen 3. Before test: 1st row at 50X magnification. After test: 2nd row at 50X magnification; 3rd row at 1000X magnification. Conditions: 72 ppm_v inhibitor, 1 wt.% NaCl aqueous solution, pH 5, pCO₂=0.97 bar, 25 °C, 16 m/s, 4 day test duration, X65 steel, O₂ < 2 ppb.

conditions were maintained the same as previous experiments. Fig. 23 shows the LPR corrosion rate results. A similar trend of general corrosion rate evolution, as compared to previous experiments, indicates that the bulk test conditions remained the same. The surface morphologies of both flat and protrusion specimens after the experiment were examined by SEM. No localized corrosion was found on neither the flat nor the protrusion specimens. They all showed a similar uniformly-corroded surface, as exemplified in Fig. 24. Therefore, the results corroborate the hypothesis that cavitation is the most likely cause of the localized corrosion observed in the previous experiments.

3.6. Mitigation of cavitation induced localized corrosion

At this stage, it was understood that cavitation was able to disrupt the adsorbed inhibitors on the metal surface and lead to pitting corrosion. This leads to the next question: can an excess amount of the same inhibitor be used to suppress this type of localized corrosion? Subsequently, an experiment with a very high inhibitor concentration was conducted (720 ppm_v inhibitor – 10 times the original concentration used in previous experiments). The specimen arrangement remained the same as shown in Fig. 5 with the protrusion specimen at the furthest downstream port (port 4) where cavitation occurred. Fig. 25 shows the LPR corrosion rates for the new 720 ppm_v inhibitor experiment compared with the previous 72 ppm_v inhibitor experiment. As expected, the similar trend indicates that general corrosion was effectively inhibited. The surface morphologies of the flat and protrusion

specimens before and after the experiments were examined. Again, no localized corrosion was observed, as shown in Fig. 26. The experimental results in this series of tests demonstrate that with an excess amount of inhibitor, the localized corrosion was mitigated, even in the presence of cavitation.

4. Discussion: mechanisms of flow/cavitation induced pitting corrosion and its mitigation

In this research, it was found so far that:

- there was no evidence of inhibitor failure due to high WSS (up to 5000 Pa);
- in the presence of the inhibitor (at 72 ppm_v), severe pitting corrosion occurred in disturbed flow, some at the leading edge and more severe at the top surface of the protrusion; this was caused by cavitation.
- using an excess amount of inhibitor (720 ppm_v), this pitting corrosion was mitigated.

While these findings seem plausible and are corroborated in a few different ways, the challenge is to explain this kind of behavior in terms of accepted theories of inhibitor adsorption.

It was previously established that the adhesion strength of the inhibitor molecules to the steel surface, is of the order of 10⁶–10⁷ Pa [42]. This can be used to explain the first point – why high WSS (up to

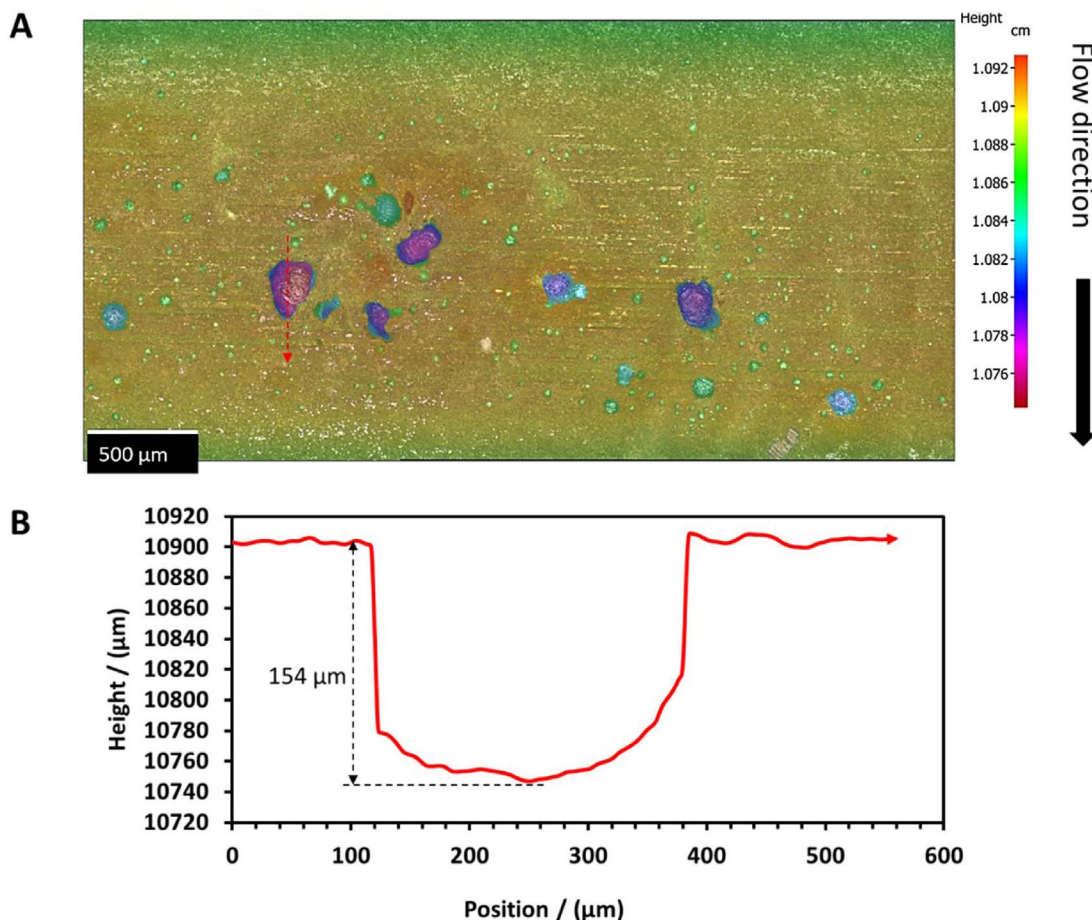


Fig. 16. (A): Profilometry image after experiment on the top of the protrusion Specimen 3; (B): depth scan across the dotted red line marked in (A). Conditions: 72 ppm_v inhibitor, 1 wt.% NaCl aqueous solution, pH 5, pCO₂=0.97 bar, 25 °C, 16 m/s, 4 day test duration, X65 steel, O₂ < 2 ppb. (For interpretation of the references to color in this figure legend, the reader is referred to the web version of this article.)

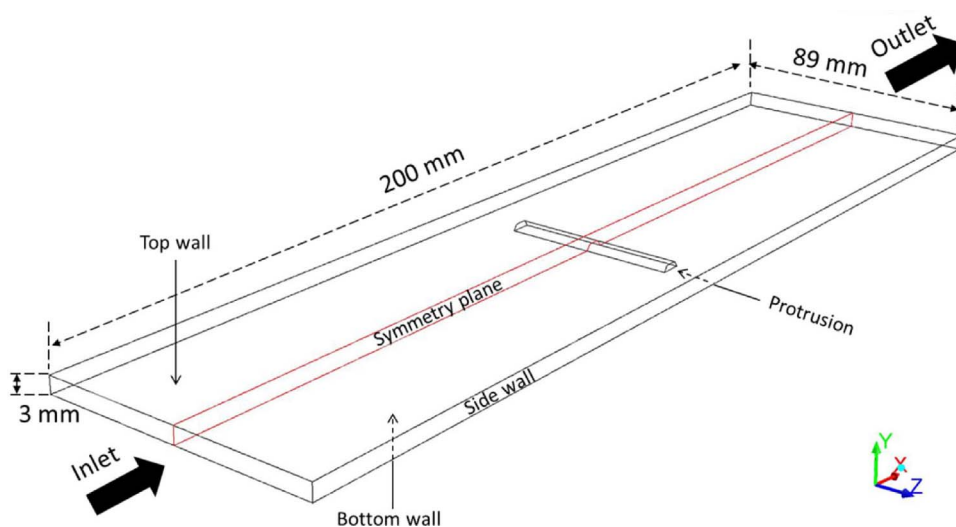


Fig. 17. Simulated flow geometry using CFD. Due to length-wise symmetry, only one half of the domain was simulated.

5000 Pa) did not lead to the failure of the inhibitor. It should be noted that 5000 Pa is already higher than typical WSS found in multiphase flow in the field [24].

It is also known that the mechanical impacts of collapsing cavitation bubbles onto a solid surface can easily reach the 10⁸–10⁹ Pa range [36,43]. Undoubtedly, this magnitude of stress can exceed the adhesion strength of the inhibitor molecules to the steel surface and mechanical removal of the inhibitor is expected. While this simple “stress magnitude based” logic is able to explain the second point – reason for

inhibitor failure at lower concentrations (72 ppm_v), it remains unclear how the performance of the inhibitor at higher concentrations (720 ppm_v) was not affected in the same way (third point). To do that, we must turn to the kinetics of adsorption/desorption process that governs inhibitor performance.

4.1. Adsorption kinetics considerations

The inhibitor adsorption/desorption is a dynamic process which

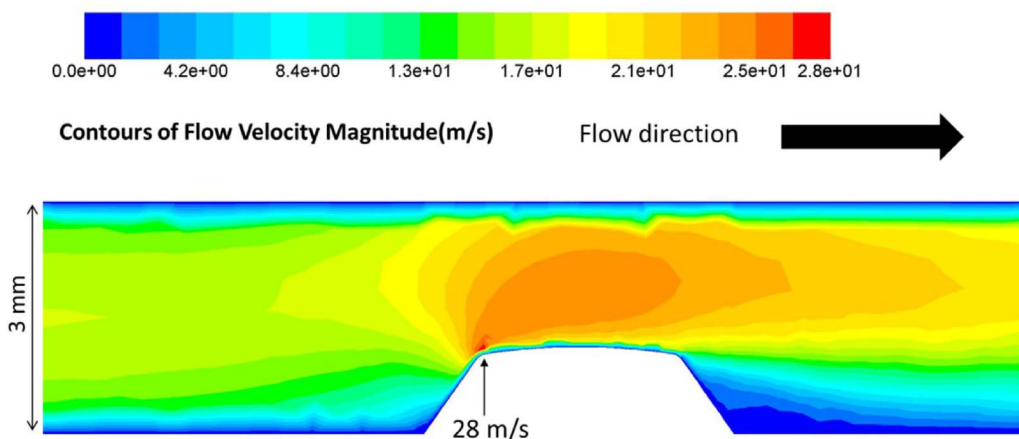


Fig. 18. A 2-D image of flow velocity magnitude distribution across the symmetry plane.

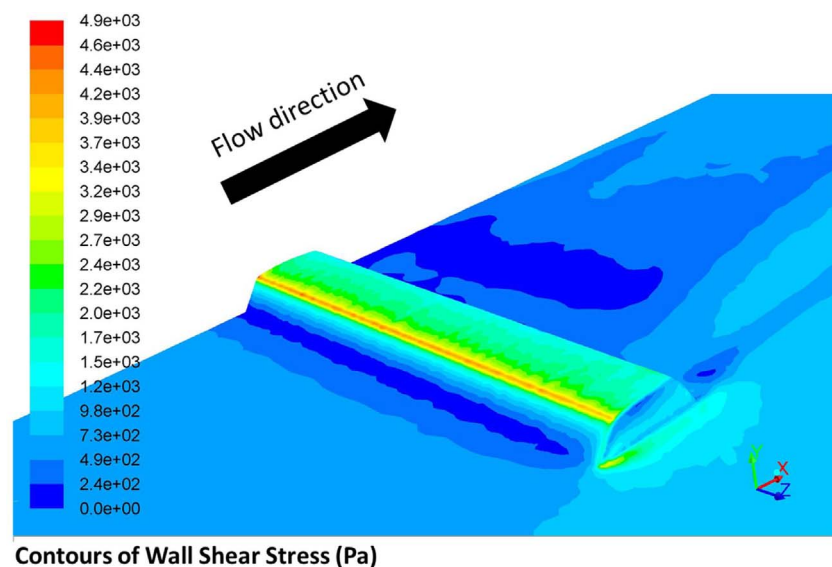


Fig. 19. A 3-D image of wall shear stress distribution at the bottom plate of the TCFC near the protrusion (due to symmetry, only half of the bottom wall is shown).

may or may not be in equilibrium. Various previous studies using similar inhibitor formulations suggest that the adsorption/desorption of imidazoline-type inhibitors follows the Langmuir adsorption model with the equilibrium described via [9,26,44–47]:

$$\left(\frac{1}{\theta} - 1\right)c_{inhib}^b = \frac{1}{K} \quad (3)$$

where c_{inhib}^b is the inhibitor concentrations in the bulk solution; θ is the surface coverage of inhibitor ($0 < \theta < 1$), and K is the inhibitor adsorption equilibrium constant, defined as:

$$K = \frac{k_{ads}}{k_{des}} \quad (4)$$

where k_{ads} and k_{des} are the reaction rate constants for adsorption and desorption processes, respectively.

A different explanation can now be made for a series of small pits found along the leading edge of the protrusion specimen at lower inhibitor concentrations (72 ppm_v), as shown in Fig. 12 and Fig. 15. As discussed in previous sections, formation of cavitation bubbles at this location created relatively large areas of gas-liquid interface that have consumed a fraction of the inhibitor molecules which are amphiphilic in nature and tend to aggregate at any available interface [27,48]. This led to a local depletion of inhibitor and consequently a lower inhibitor coverage on the steel surface, what caused some localized corrosion. This can be easily expressed mathematically by looking at Eq. (3): if the bulk concentration of inhibitor (c_{inhib}^b) at the leading edge is reduced due to the parasitic consumption by cavitation bubbles, and assuming that

the adsorption equilibrium constant (K) remains unchanged, this yields a decrease in surface coverage by inhibitor (θ). Due to intense turbulent mixing, the local depletion in inhibitor concentration vanishes immediately downstream of the leading edge, and no pitting was found there.

Further downstream, at the middle section of the protrusion top surface is where the most severe pitting was found, caused by cavitation bubble collapse. The dynamics of cavitation bubbles near a solid wall has been extensively researched [36,43,49–51]. During bubble collapse, the potential energy of vaporous bubbles can be converted into mechanical energy (including shock waves), but also heat, chemical energy, sound and even light emissions [43,52]. It is assumed that this energy, released in various forms during bubble collapse, impacted the steel surface and enhanced the rate of inhibitor removal, i.e. desorption (increased k_{des}). This leads to a decrease in inhibitor adsorption equilibrium constant (K) (see Eq. (4)), and with the bulk concentration of the inhibitor remaining the same, this results in a decreasing surface coverage of inhibitor (θ) according to Eq. (3).

Besides releasing high magnitude mechanical energy, collapsing cavitation bubbles can also locally release an enormous amount of heat (thermal energy), which is dissipated rapidly [53–55]. The temperature surrounding the collapsing cavitation bubbles is reported to reach several thousands of Kelvins [52,56]. Therefore, it is also possible that some of the locally released heat is transferred to the steel surface, resulting in a local temperature increase. It is found in the literature that, when the temperature increases, the desorption reaction of

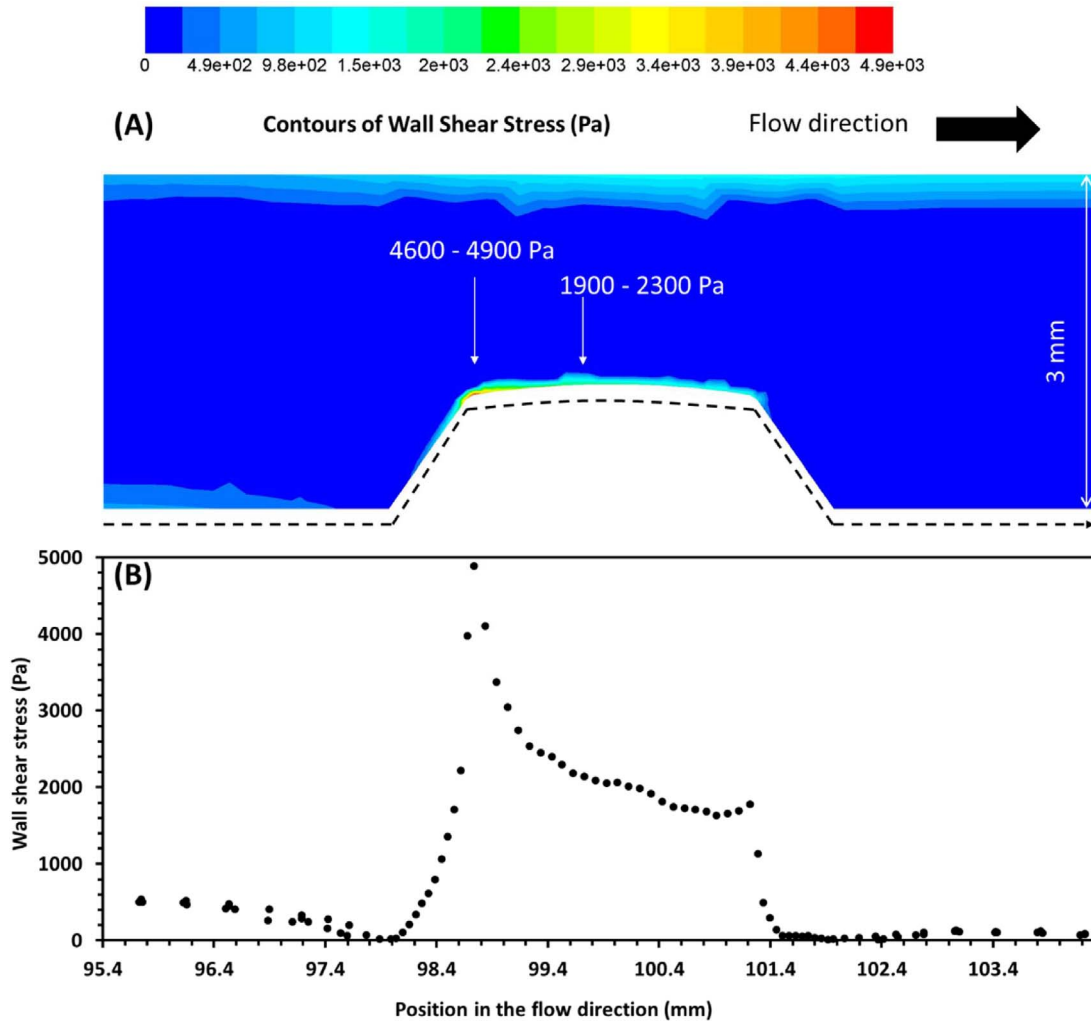


Fig. 20. Wall shear stress distribution near the protrusion: (A) 2-D image across the symmetry plane; (B) the corresponding line scan on the bottom wall at the symmetry plane, as highlighted by the black dashed line shown in (A).

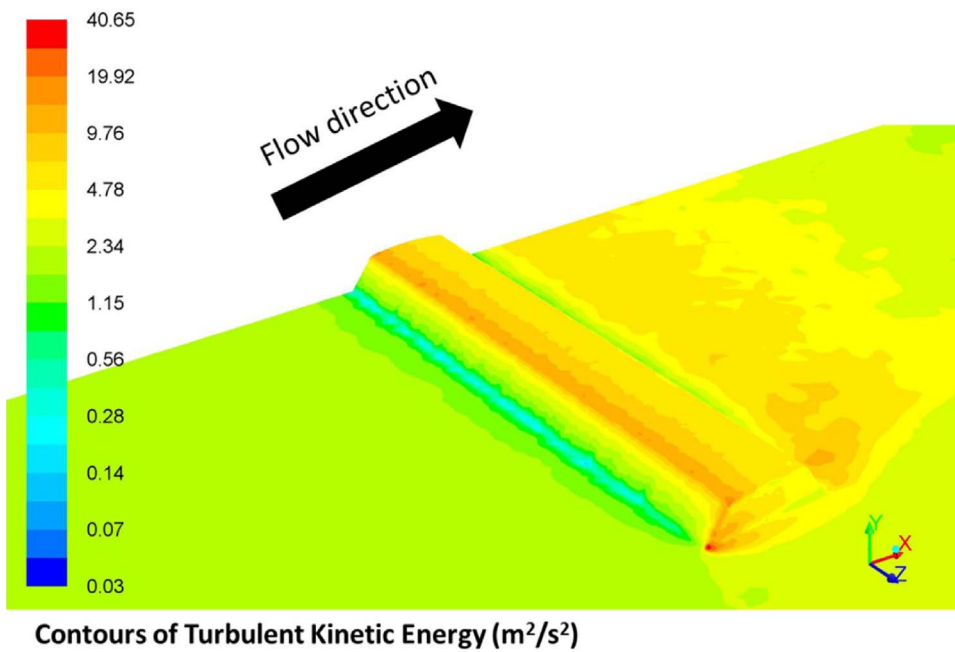


Fig. 21. A 3-D image of turbulent kinetic energy distribution at the bottom plate of the TCFC near the protrusion (due to symmetry, only half of the bottom wall is shown).

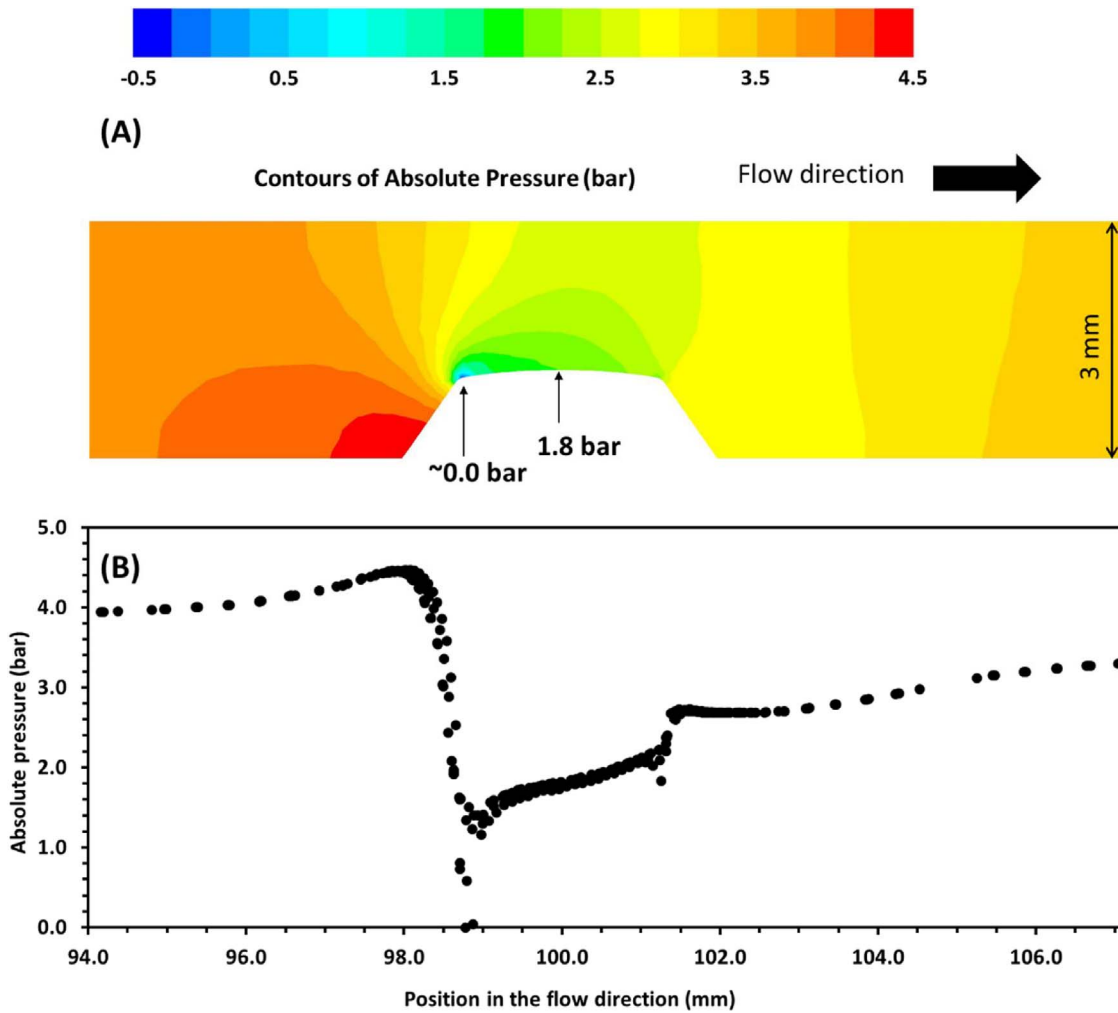


Fig. 22. Absolute (total) pressure distribution: (A): 2-D image across the symmetry plane; (B): line scan on the bottom wall at the symmetry plane.

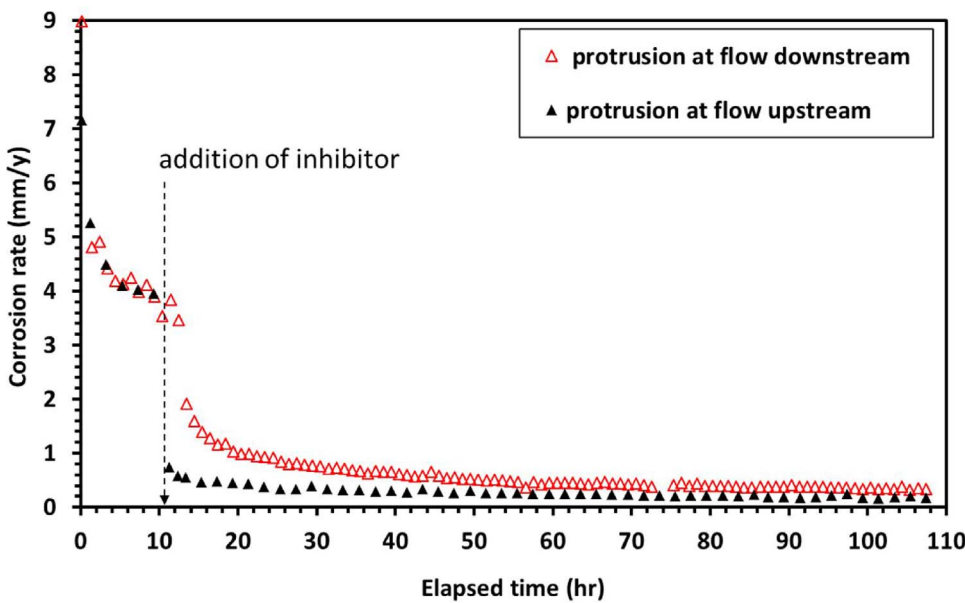


Fig. 23. LPR corrosion rates for the 72 ppm_v inhibitor tests with the protrusion specimen at two different locations in the TCFC. Conditions: 1 wt.% NaCl aqueous solution, pH 5, pCO₂=0.97 bar, 25 °C, 16 m/s, 4 day test duration, X65 steel, O₂ < 2 ppb.

imidazoline-type inhibitors is favored (k_{des} increases more than k_{ads}) [9,45,57]. Therefore, according to Eq. (4) this also leads to a decrease of K , and for the same bulk concentration of inhibitor (c_{inhib}^b), the surface coverage of inhibitor (θ) decreases, according to Eq. (3).

The same line of reasoning can now be used to explain how using an excess amount of inhibitor (720 ppm_v), was able to mitigate the pitting corrosion due to cavitation. In the explanation above, we first postulated that the parasitic consumption of the inhibitor at the leading edge

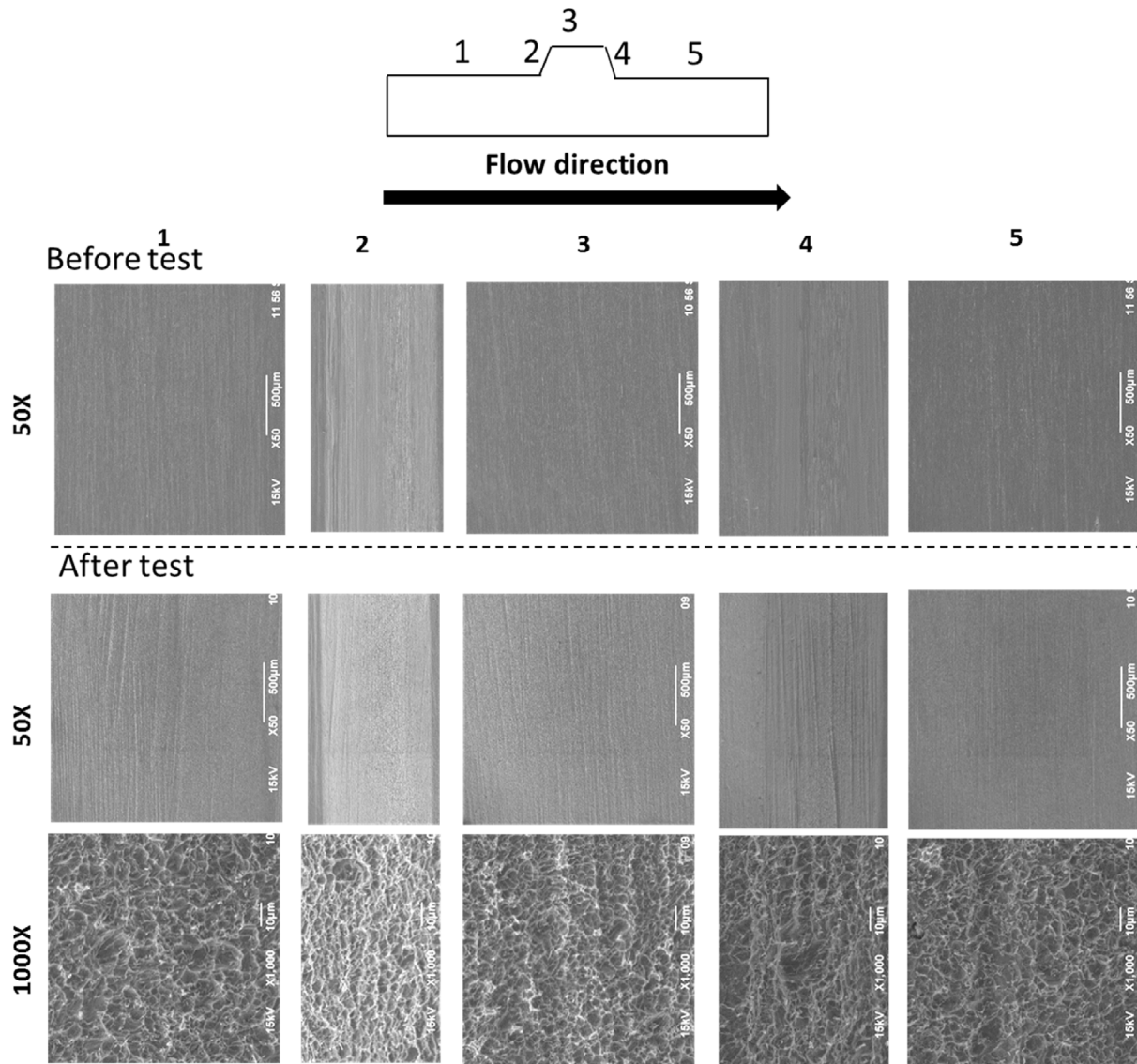


Fig. 24. SEM images of the protrusion Specimen 3 placed in the furthest upstream port of the TCFC test section (port 1). Before test: 1st row at 50X magnification. After test: 2nd row at 50X magnification; 3rd row at 1000X magnification. Conditions: 72 ppm, inhibitor, 1 wt.% NaCl aqueous solution, pH 5, $p\text{CO}_2=0.97$ bar, 25 °C, 16 m/s, 4 day test duration, X65 steel, $\text{O}_2 < 2$ ppb.

led to lower local inhibitor concentrations (c_{inhib}^b) and lower surface coverage by the inhibitor (θ), leading to pitting. It is obvious that significantly increasing the concentration of the inhibitor in the system is able to reverse this effect. Second, we suggested that energy (mechanical and/or thermal) released by the collapsing cavitation bubbles led to an increase in the rate of inhibitor desorption over adsorption, resulting in a lower adsorption equilibrium constant (K) and lower inhibitor surface coverage (θ), for the same bulk concentration (c_{inhib}^b). Again, by inspecting Eq. (3), we can see how increasing the inhibitor concentration (c_{inhib}^b) leads to a higher coverage (θ), even if the adsorption equilibrium constant (K) remains low due to increased desorption rate caused by cavitation bubble collapse.

4.2. Energy considerations

In the discussion above, we made an ad-hoc assumption that the bursts of energy released by the collapsing cavitation bubbles in the vicinity of the surface would lead to an increased rate of inhibitor desorption. While being intuitive, this statement needs some more theoretical explanation.

The adsorption/desorption reaction rate constants (k_{ads} and k_{des}) in

Eq. (4) can be written in terms of corresponding activation energies (ΔG_{ads}^\ddagger and ΔG_{des}^\ddagger) using an Arrhenius-type equation [58,59]:

$$k_{ads} = Ae^{\left(-\frac{\Delta G_{ads}^\ddagger}{RT}\right)} \quad (5)$$

$$k_{des} = De^{\left(-\frac{\Delta G_{des}^\ddagger}{RT}\right)} \quad (6)$$

where A and D are the pre-exponential factors for the adsorption and desorption reaction rate expression, respectively.

A potential energy diagram [27,58,59] can best illustrate the relationship between the adsorption and desorption activation energy (ΔG_{ads}^\ddagger and ΔG_{des}^\ddagger) as related via the thermodynamic free energy change ($\Delta_{rxn}G^\circ$) for inhibitor adsorption/desorption. It has been found that the standard free energy change due to surfactant inhibitor adsorption reaction ($\Delta_{rxn}G^\circ$) is approximately in the range -20 kJ to -40 kJ per mole of adsorbed inhibitors [47,60,61]. This suggests that the adsorption reaction is thermodynamically favored at standard conditions. The activation energy of the inhibitor adsorption reaction (ΔG_{ads}^\ddagger) is estimated to be approximately 20 kJ per mole of inhibitor [62,63]. According to this, the desorption activation energy (ΔG_{des}^\ddagger) should be in

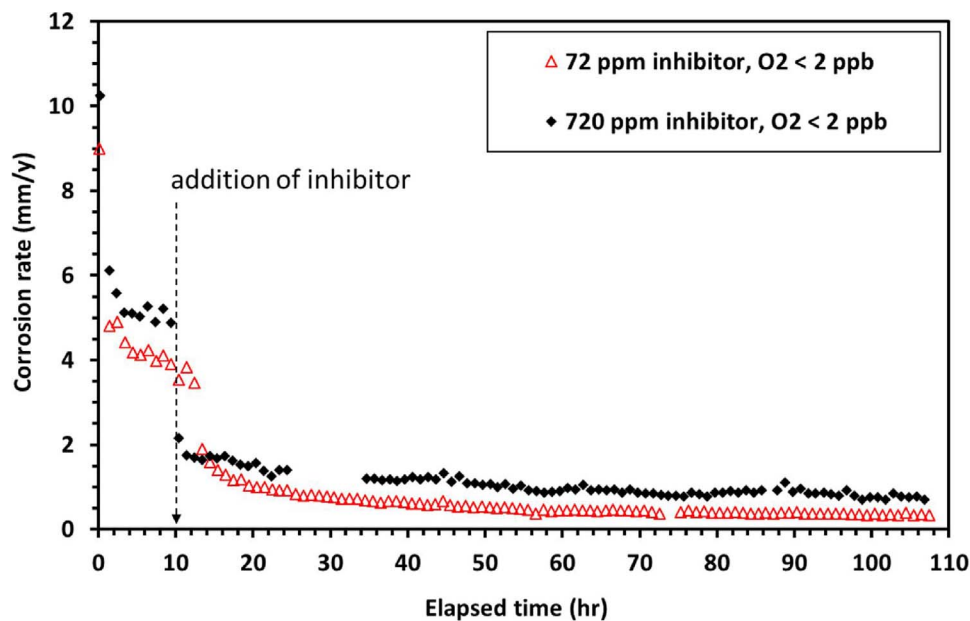


Fig. 25. LPR corrosion rates with various inhibitor concentrations. Conditions: 1 wt.% NaCl aqueous solution, pH 5, $pCO_2=0.97$ bar, 25 °C, 16 m/s, 4 day test duration, X65 steel, $O_2 < 2$ ppb.

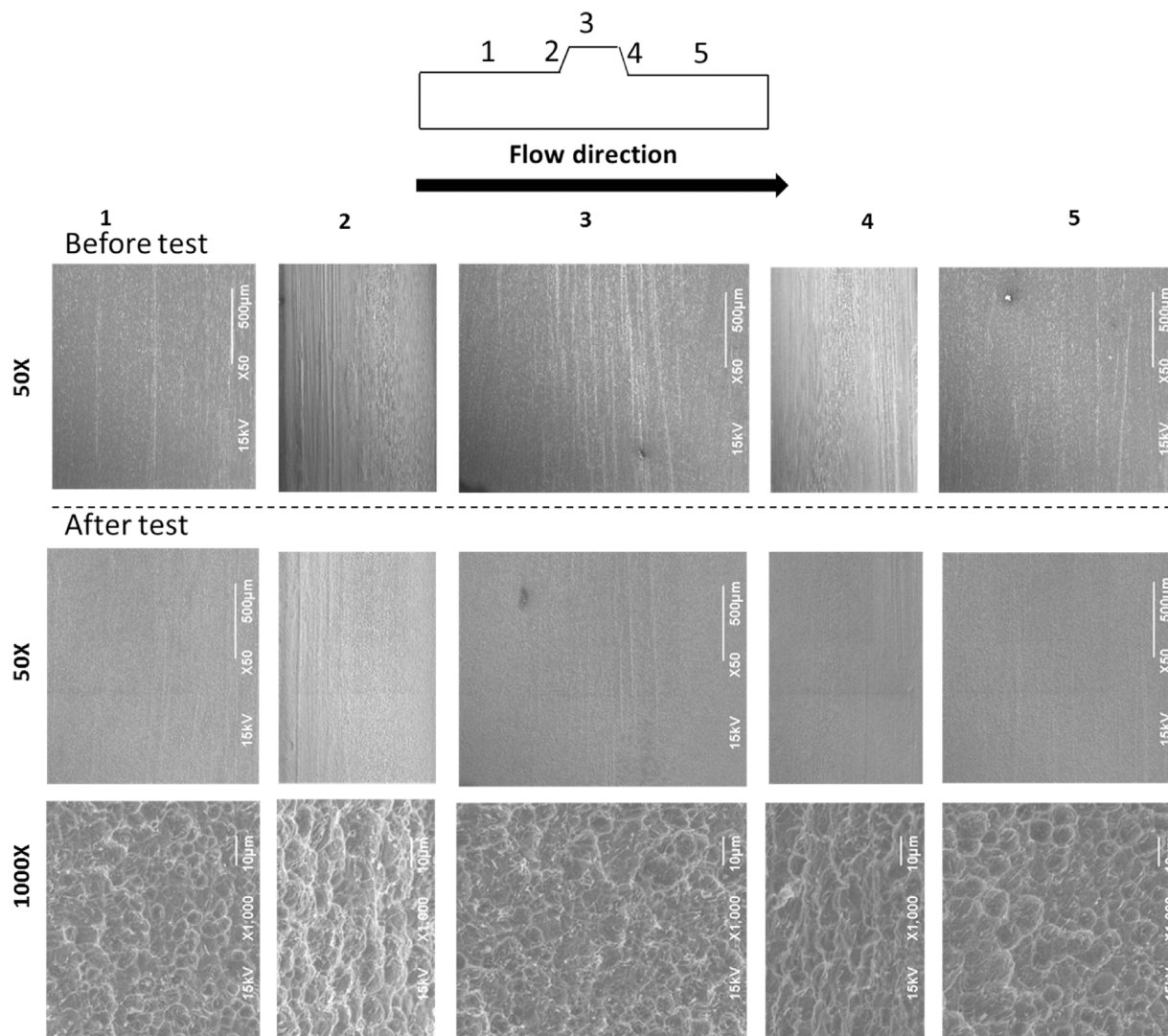


Fig. 26. SEM images of the protrusion Specimen 3. Before test: 1st row at 50X magnification. After test: 2nd row at 50X magnification; 3rd row at 1000X magnification. Conditions: 720 ppm_v inhibitor, 1 wt.% NaCl aqueous solution, pH 5, $pCO_2=0.97$ bar, 25 °C, 16 m/s, 4 day test duration, X65 steel, $O_2 < 2$ ppb.

the range: 40 kJ to 60 kJ per mole of adsorbed inhibitors.

Due to interaction with the flow and/or due to cavitation, the surface energy level of the adsorbed inhibitor molecules is increased by amount E , thereby decreasing the required desorption activation energy (ΔG_{des}^\ddagger). One can now calculate the new desorption rate constant accounting for the cavitation energy input as:

$$k_{des}' = De^{\left[-\frac{(\Delta G_{des}^\ddagger - E)}{RT} \right]} \quad (7)$$

where E is the energy input felt by the adsorbed inhibitor layer at the surface due to flow and/or collapsing cavitation bubbles. When substituting the new increased reaction rate constant into Eq. (4), the adsorption/desorption reaction equilibrium shifts in favor of the desorption reaction making the equilibrium constant (K) decrease, the surface coverage of inhibitor decreases as well, which explains the localized inhibitor failure.

The magnitude of the total energy E that the flow can exert on the adsorbed inhibitor molecules now can be estimated. Firstly, the thermal energy of a given system which can be represented on a molecular level by the translational kinetic energy of the randomly moving molecules (E_t), expressed on a molar basis in J/mol as [64]:

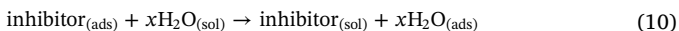
$$E_t = \frac{3}{2}RT \quad (8)$$

where R is the gas constant and T is the absolute temperature (K). For the present case: the bulk temperature 298 K the thermal energy is calculated to be $E_t = 3.7$ kJ/mol.

There is also an ordered directional movement of the molecules due to the mean flow and the associated kinetic energy (E_k) can be calculated from the bulk flow velocity as:

$$E_k = \frac{1}{2}mv^2 \quad (9)$$

where m is the molar mass of liquid molecules (kg/mol); and v is the flow velocity (m/s). For the present case: mean flow velocity of 25 m/s (see Fig. 18), the mean flow kinetic energy is calculated to be $E_k = 5.6$ J/mol of water. The turbulent kinetic energy of the flow can also be considered by using the maximum value calculated by CFD to be approximately $10 \text{ m}^2/\text{s}^2$ at the top of the protrusion, as seen in Fig. 21. This yields 0.18 J/mol of water. It is noted that the turbulent kinetic energy is much smaller than the mean flow kinetic energy or the thermal energy. To associate this amount of energy with the adsorbed inhibitor, one can assume that the process of inhibitor desorption essentially involves the displacement of an adsorbed inhibitor molecule by x water molecules [65]:



with the stoichiometric coefficient x being a relatively small number of the order of unity. Therefore, if the total energy (thermal and flow) of a given number of moles of water is transferred to the equivalent number of moles of adsorbed inhibitor, this will amount to about $E = 3.7$ kJ/mol of adsorbed inhibitor. This shows that the energy level of the bulk flow (including thermal and kinetic energy) is several orders of magnitude lower than the desorption activation energy, which is in the range of 10^4 – 10^5 J/mol of adsorbed inhibitor. It therefore seems theoretically impossible to expect that the bulk flow could contribute to mechanical removal of adsorbed inhibitors, at least not under the present conditions. This is exactly what was found in the experimental portion of this study, as described above. Due to the large gap involved in the required energy levels (1–2 orders of magnitude), it is probably fair to generalize that under most field conditions, one should not expect that flow and associated WSS would lead to failure of corrosion inhibitor films.

However, collapsing cavitating bubbles certainly do not fall into this category, when looking into the level of energy transferred to an adsorbed inhibitor film by collapsing cavitation bubbles. The potential

energy (E_p) of a single spherical cavitation bubble is given by [36]:

$$E_p = \frac{4}{3}\pi r^3(P_\infty - P_v) \quad (11)$$

where P_∞ is the environmental pressure at infinite distance from the bubble; P_v is the vapor pressure of the liquid; and r is the bubble radius. The potential energy on a molar basis may be written as:

$$E_p' = \frac{m}{\rho_v}(P_\infty - P_v) \quad (12)$$

where m is the molar mass of the liquid (kg/mol); and ρ_v is the vapor density of the liquid (kg/m³). At 298 K, the vapor pressure and vapor density of water are 3200 Pa and 0.023 kg/m³, respectively. The ambient pressure at infinite distance was of the order of 10^5 Pa. Consequently, the cavitating bubble potential energy is calculated to be approximately 75 kJ/mol of water vapor. If we assume a similar stoichiometry as above (reaction (10)), then we can conclude that the potential energy released by the collapsing cavitation bubbles is in the same range as the activation energy required for inhibitor desorption. Despite the coarse nature of this order-of-magnitude calculations, it seems quite plausible that collapse of cavitating bubbles could significantly affect inhibitor desorption and consequently the surface coverage, leading to pitting, what was actually observed in the present study.

It can be now stated that the notion that mechanical forces due to flow (such as those giving rise to high WSS) can lead to failure of adsorbed inhibitor films seems to be a myth, at least when considering typical single-phase and multiphase flow patterns found in the field and when dealing with conventional inhibitors that are properly applied. The exceptions are specific conditions when cavitation happens.

Cavitation by water vapor bubbles can happen only in low pressure sections of a given system, such as at inlet sections of lines leading to pumps and compressors. However, cavitation by condensable hydrocarbons, when close to their saturation point, can also be considered a hazardous situation, since equally large forces can be created by collapsing hydrocarbon vapor bubbles, which could damage the inhibitor film and lead to localized corrosion. This condition is quite common in multiphase lines and gas transportation lines. Transfer lines in refineries are another example.

5. Conclusions

Based on the presented results and discussion, several conclusions can be drawn:

- 1) There was no evidence of inhibitor failure due to high wall shear stress (up to 5000 Pa)
- 2) In the presence of the inhibitor (at 72 ppm_v), severe pitting corrosion occurred in disturbed flow, which was caused by cavitation of condensable water vapor bubbles.
- 3) Using an excess amount of inhibitor (720 ppm_v), this pitting corrosion was mitigated.
- 4) The observed behavior can be readily explained in terms of the kinetics of inhibitor adsorption/desorption and the associated activation energy analysis.

Acknowledgements

This research is based on part of W. Li's PhD dissertation at Ohio University [27]. The research was financially sponsored from the Corrosion Center Joint Industry Project in the Institute for Corrosion and Multiphase Technology at Ohio University. The authors thank Dr. David Young for helpful discussions.

References

- [1] S. Nescic, W. Sun, Corrosion in acid gas solutions, in: J.A. Richardson, et al. (Ed.), *Shreir's Corrosion*, Elsevier Amsterdam, The Netherlands, 2010, pp. 1270–1298.
- [2] H. Tian, W. Li, B. Hou, D. Wang, Insights into corrosion inhibition behavior of multi-active compounds for X65 pipeline steel in acidic oilfield formation water, *Corros. Sci.* 117 (2017) 43–58.
- [3] Y. Tan, M. Mocerino, T. Paterson, Organic molecules showing the characteristics of localised corrosion aggravation and inhibition, *Corros. Sci.* 53 (2011) 2041–2045.
- [4] Y. Zuo, L. Yang, Y. Tan, Y. Wang, J. Zhao, The effects of thioureido imidazoline and NaNO₂ on passivation and pitting corrosion of X70 steel in acidic NaCl solution, *Corros. Sci.* 120 (2017) 99–106.
- [5] H. Liu, T. Gu, G. Zhang, W. Wang, S. Dong, Y. Cheng, H. Liu, Corrosion inhibition of carbon steel in CO₂-containing oilfield produced water in the presence of iron-oxidizing bacteria and inhibitors, *Corros. Sci.* 105 (2016) 149–160.
- [6] Y. Tang, F. Zhang, S. Hu, Z. Cao, Z. Wu, W. Jing, Novel benzimidazole derivatives as corrosion inhibitors of mild steel in the acidic media. Part I: Gravimetric, electrochemical, SEM and XPS studies, *Corros. Sci.* 74 (2013) 271–282.
- [7] B. Wang, M. Du, J. Zhang, C.J. Gao, Electrochemical and surface analysis studies on corrosion inhibition of Q235 steel by imidazoline derivative against CO₂ corrosion, *Corros. Sci.* 53 (2011) 353–361.
- [8] L. Zeng, G.A. Zhang, X.P. Guo, C.W. Chai, Inhibition effect of thioureidoimidazoline inhibitor for the flow accelerated corrosion of an elbow, *Corros. Sci.* 90 (2015) 202–215.
- [9] S. Ramachandran, B.-L. Tsai, M. Blanco, H. Chen, Y. Tang, W.A. Goddard III, Self-assembled monolayer mechanism for corrosion inhibition of iron by imidazolines, *Langmuir* 12 (1996) 6419–6428.
- [10] S. Nescic, Effects of multiphase flow on internal CO₂ corrosion of mild steel pipelines, *Energy Fuels* 26 (2012) 4098–4111.
- [11] T. Hara, H. Asahi, Y. Suehiro, H. Kaneta, Effect of flow velocity on carbon dioxide corrosion behavior in oil and gas environments, *Corrosion* 56 (2000) 860–866.
- [12] Q. Li, H. Hu, Y.F. Cheng, Corrosion of pipelines in CO₂-saturated oil-water emulsion flow studied by electrochemical measurements and computational fluid dynamics modeling, *J. Petrol. Sci. Eng.* 147 (2016) 408–415.
- [13] D.M. Ortega-Toledo, J.G. Gonzalez-Rodriguez, M. Casales, L. Martinez, A. Martinez-Villafane, CO₂ corrosion inhibition of X-120 pipeline steel by a modified imidazoline under flow conditions, *Corros. Sci.* 53 (2011) 3780–3787.
- [14] W. Li, Y. Xiong, B. Brown, K.E. Kee, S. Nescic, Measurement of wall shear stress in multiphase flow and its effect on protective FeCO₃ corrosion product layer removal, NACE International CORROSION 2015 Conference, 2015, Paper No. 5922 (2015).
- [15] W. Li, J. Landon, B. Irvin, L. Zheng, K. Ruh, L. Kong, J. Pelgen, D. Link, J.D. Figueroa, J. Thompson, H. Nikolic, K. Liu, Use of carbon steel for construction of post-combustion CO₂ capture facilities: a pilot-scale corrosion study, *Ind. Eng. Chem. Res.* 56 (2017) 4792–4803.
- [16] W. Li, B. Brown, D. Young, S. Nescic, Investigation of pseudo-passivation of mild steel in CO₂ corrosion, *Corrosion* 70 (2014) 294–302.
- [17] C.M. Canto Maya, Effect of Wall Shear Stress on Corrosion Inhibitor Film Performance PhD Dissertation, Ohio University, 2015.
- [18] E. Gulbrandsen, J. Kvaerckval, Effect of oil-in-water emulsions on the performance of carbon dioxide corrosion inhibitors, *Corrosion* 63 (2007) 187–196.
- [19] R.H. Hausler, G. Schmitt, Hydrodynamic and flow effects on corrosion inhibition, NACE International CORROSION 2004 Conference, 2004, Paper No.04402. (2004).
- [20] B.F.M. Pots, E.L.J.A. Hendriksen, H.A.M. de Reus, H.B. Pit, S.J. Paterson, Field study of corrosion inhibition at very high flow velocity, NACE International CORROSION 2003 Conference, 2003, Paper No. 03321. (2003).
- [21] J.H. Gerretsen, A. Visser, Inhibitor performance under liquid droplet impingement conditions in CO₂-containing environment, *Corros. Sci.* 34 (1993) 1299–1310.
- [22] E. Gulbrandsen, A. Grana, Testing of carbon dioxide corrosion inhibitor performance at high flow velocities in jet impingement geometry. Effects of mass transfer and flow forces, *Corrosion* 63 (2007) 1009–1020.
- [23] S. Nescic, G.T. Solvi, S. Skjerve, Comparison of rotating cylinder and loop methods for testing CO₂ corrosion inhibitors, *Brit. Corros. J.* 32 (1997) 269–276.
- [24] W. Li, B.F.M. Pots, B. Brown, K.E. Kee, S. Nescic, A direct measurement of wall shear stress in multiphase flow – Is it an important parameter in CO₂ corrosion of carbon steel pipelines? *Corros. Sci.* 110 (2016) 35–45.
- [25] W. Li, Investigation of Pseudo-passive Layer Formation in CO₂ Corrosion Master's Thesis, Ohio University, 2011.
- [26] M.A.J. Mazumder, H.A. Al-Muallem, S.A. Ali, The effects of N-pendants and electron-rich amidine motifs in 2-(p-alkoxyphenyl)-2-imidazolines on mild steel corrosion in CO₂-saturated 0.5 M NaCl, *Corros. Sci.* 90 (2015) 54–68.
- [27] W. Li, Mechanical Effects of Flow on CO₂ Corrosion Inhibition of Carbon Steel Pipelines PhD Dissertation, Ohio University, 2016.
- [28] A. Edwards, C. Osborne, S. Webster, D. Klenerman, M. Joseph, P. Ostovar, M. Doyle, Mechanistic studies of the corrosion inhibitor oleic imidazoline, *Corros. Sci.* 36 (1994) 315–325.
- [29] Y. Xiong, AFM Studies of the Metallicity of Single-walled Carbon Nanotubes and Corrosion Inhibitor Adsorption PhD Dissertation, Ohio University, 2011.
- [30] I. Jevremovic, M. Singer, M. Achour, D. Blumer, T. Baugh, V. Miskovic-Stankovic, S. Nescic, A novel method to mitigate the top-of-the-line corrosion in wet gas pipelines by corrosion inhibitor within a foam matrix, *Corrosion* 69 (2013) 186–192.
- [31] D.A. Jones, Principles and Prevention of Corrosion, second ed., Prentice Hall, Upper Saddle River, NJ, 1996.
- [32] S. Nescic, Carbon dioxide corrosion of mild steel, in: R. Winston Revie (Ed.), *Uhlig's Corrosion Handbook*, third ed., John Wiley & Sons, Inc, Hoboken, New Jersey, 2011, pp. 229–245.
- [33] R. Barker, X. Hu, A. Neville, S. Cushnaghan, Assessment of preferential weld corrosion of carbon steel pipework in CO₂-saturated flow-induced corrosion environments, *Corrosion* 69 (2013) 1132–1143.
- [34] D.F. Young, B.R. Munson, T.H. Okishi, A Brief Introduction to Fluid Mechanics, John Wiley & Sons, Inc, New York NY, 1997.
- [35] C.H.M. Baltis, C.W.M. van der Geld, Heat transfer mechanisms of a vapour bubble growing at a wall in saturated upward flow, *J. Fluid Mech.* 771 (2015) 264–302.
- [36] A. Vogel, W. Lauterborn, R. Timm, Optical and acoustic investigations of the dynamics of laser-produced cavitation bubbles near a solid boundary, *J. Fluid Mech.* 206 (1989) 299–338.
- [37] I. Akhatov, O. Lindau, A. Topolnikov, R. Mettin, N. Vakhitova, W. Lauterborn, Collapse and rebound of a laser-induced cavitation bubble, *Phys. Fluids* 13 (2001) 2805–2819.
- [38] S.-H. Yang, S.-Y. Jaw, K.-C. Yeh, Single cavitation bubble generation and observation of the bubble collapse flow induced by a pressure wave, *Exp. Fluids* 47 (2009) 343–355.
- [39] D. Carnelli, A. Karimi, J.-P. Franc, Evaluation of the hydrodynamic pressure of cavitation impacts from stress-strain analysis and geometry of individual pits, *Wear* 289 (2012) 104–111.
- [40] A.S. Grinspan, R. Gnanamoorthy, Development of a novel oil cavitation jet peening system and cavitation jet erosion in aluminum alloy AA 6063-T6, *J. Fluids Eng.* 131 (2009) 061301-1–061301-8.
- [41] I. Tzanakis, D.G. Eskin, A. Georgoulas, D.K. Fytanidis, Incubation pit analysis and calculation of the hydrodynamic impact pressure from the implosion of an acoustic cavitation bubble, *Ultrason. Sonochem.* 21 (2014) 866–878.
- [42] Y. Xiong, B. Brown, B. Kinsella, S. Nescic, A. Pailleret, Atomic force microscopy study of the adsorption of surfactant corrosion inhibitor films, *Corrosion* 70 (2014) 247–260.
- [43] A. Philipp, W. Lauterborn, Cavitation erosion by single laser-produced bubbles, *J. Fluid Mech.* 361 (1998) 75–116.
- [44] I. Jevremovic, M. Singer, S. Nescic, V. Miskovic-Stankovic, Inhibition properties of self-assembled corrosion inhibitor talloil diethylenetriamine imidazoline for mild steel corrosion in chloride solution saturated with carbon dioxide, *Corros. Sci.* 77 (2013) 265–272.
- [45] X. Zhang, F. Wang, Y. He, Y. Du, Study of the inhibition mechanism of imidazoline amide on CO₂ corrosion of Armo iron, *Corros. Sci.* 43 (2001) 1417–1431.
- [46] J. Zhao, G. Chen, The synergistic inhibition effect of oleic-based imidazoline and sodium benzoate on mild steel corrosion in a CO₂-saturated brine solution, *Electrochim. Acta* 69 (2012) 247–255.
- [47] K. Zhang, B. Xu, W. Yang, X. Yin, Y. Liu, Y. Chen, Halogen-substituted imidazoline derivatives as corrosion inhibitors for mild steel in hydrochloric acid solution, *Corros. Sci.* 90 (2015) 284–295.
- [48] M.J. Rosen, Surfactants and Interfacial Phenomena, third ed., John Wiley & Sons, Inc, Hoboken New Jersey, 2004.
- [49] A. Vogel, S. Busch, U. Parlitz, Shock wave emission and cavitation bubble generation by picosecond and nanosecond optical breakdown in water, *J. Acoust. Soc. Am.* 100 (1996) 148–165.
- [50] J.-C. Isselin, A.-P. Alloncle, M. Autric, On laser induced single bubble near a solid boundary: contribution to the understanding of erosion phenomena, *J. Appl. Phys.* 84 (1998) 5766–5771.
- [51] R. Fortes-Patella, G. Challier, J.L. Reboud, A. Archer, Energy balance in cavitation erosion: from bubble collapse to indentation of material surface, *J. Fluids Eng.* 135 (2013) 011303-1–011303-11.
- [52] Y.T. Didenko, K.S. Suslick, The energy efficiency of formation of photons, radicals and ions during single-bubble cavitation, *Nature* 418 (2002) 394–397.
- [53] T.J. Matula, Inertial cavitation and single-bubble sonoluminescence, *Phil. Trans. R. Soc. Lond. A* 357 (1999) 225–249.
- [54] J. Lee, S. Kentish, T.J. Matula, M. Ashokkumar, Effect of surfactants on inertial cavitation activity in a pulsed acoustic field, *J. Phys. Chem. B* 109 (2005) 16860–16865.
- [55] Y.T. Didenko, W.B. McNamara III, K.S. Suslick, Hot spot conditions during cavitation in water, *J. Am. Chem. Soc.* 121 (1999) 5817–5818.
- [56] E.B. Flint, K.S. Suslick, The temperature of cavitation, *Science* 253 (1991) 1397–1399.
- [57] G. Zhang, C. Chen, M. Lu, C. Chai, Y. Wu, Evaluation of inhibition efficiency of an imidazoline derivative in CO₂-containing aqueous solution, *Mater. Chem. Phys.* 105 (2007) 331–340.
- [58] P. Atkins, J. de Paula, Physical Chemistry, eighth ed., Oxford University Press, Great Britain, 2006.
- [59] D.D. Ebbing, S.D. Gammon, General Chemistry, ninth ed., Houghton Mifflin Company, Boston, MA, 2009.
- [60] W. Durnie, R. de Marco, A. Jefferson, B. Kinsella, Development of a structure-activity relationship for oil field corrosion inhibitors, *J. Electrochem. Soc.* 146 (1999) 1751–1756.
- [61] F. Bentiss, M. Lebrini, M. Lagrenee, Thermodynamic characterization of metal dissolution and inhibitor adsorption processes in mild steel/2,5-bis(n-thienyl)-1,3,4-thiadiazoles/hydrochloric acid system, *Corros. Sci.* 47 (2005) 2915–2931.
- [62] A. Honciuc, D.J. Baptiste, L.P. Campbell, D.K. Schwartz, Solvent dependence of the activation energy of attachment determined by single molecule observations of surfactant adsorption, *Langmuir* 25 (2009) 7389–7392.
- [63] A. Honciuc, A.L. Howard, D.K. Schwartz, Single molecule observations of fatty acid adsorption at the silica/water interface: activation energy of attachment, *J. Phys. Chem. C* 113 (2009) 2078–2081.
- [64] G. Chen, Nanoscale Energy Transport and Conversion: a Parallel Treatment of Electrons, Molecules, Phonons, and Photons, Oxford University Press, Inc, New York NY, 2005.
- [65] J.O.M. Bockris, D.A.J. Swinkels, Adsorption of n-decylamine on solid metal electrodes, *J. Electrochem. Soc.* 111 (1964) 736–743.